Check for updates

ADVANCING EARTH AND SPACE SCIENCES

JGR Earth Surface

RESEARCH ARTICLE
10.1029/2023JF007452

Key Points:

- We developed a 1D model for permafrost riverbank erosion across the thaw- and entrainment-limited regimes
- When a thawed sediment layer develops, it tends toward a constant thickness where sediment entrainment and permafrost thaw rates balance
- Periodic thaw-layer failure produces bank erosion rates that simultaneously depend on sediment entrainment and permafrost thaw rates

Supporting Information:

Supporting Information may be found in the online version of this article.

Correspondence to:

M. M. Douglas,
madisond@mit.edu

Citation:

Douglas, M. M., & Lamb, M. P. (2024). A model for thaw and erosion of permafrost riverbanks. *Journal of Geophysical Research: Earth Surface*, *129*, e2023JF007452. https://doi.org/10.1029/2023JF007452

Received 16 SEP 2023
Accepted 31 JAN 2024

© 2024. American Geophysical Union. All Rights Reserved.

A Model for Thaw and Erosion of Permafrost Riverbanks

Madison M. Douglas[1,2] **and Michael P. Lamb**[1]

[1]Division of Earth and Planetary Sciences, California Institute of Technology, Pasadena, CA, USA, [2]Department of Earth, Atmospheric, and Planetary Sciences, Massachusetts Institute of Technology, Cambridge, MA, USA

Abstract

How will bank erosion rates in Arctic rivers respond to a warming climate? Existing physical models predict that bank erosion rates should increase with water temperature as permafrost thaws more rapidly. However, the same theory predicts much faster erosion than is typically observed. We propose that these models are missing a key component: a layer of thawed sediment on the bank that buffers heat transfer and slows erosion. We developed a 1D model for this thawed layer, which reveals three regimes for permafrost riverbank erosion. Thaw-limited erosion occurs in the absence of a thawed layer, such that rapid pore-ice melting sets the pace of erosion, consistent with existing models. Entrainment-limited erosion occurs when pore-ice melting outpaces bank erosion, resulting in a thawed layer, and the relatively slow entrainment of sediment sets the pace of erosion similar to non-permafrost rivers. Third, the intermediate regime occurs when the thawed layer goes through cycles of thickening and failure, leading to a transient thermal buffer that slows thaw rates. Distinguishing between these regimes is important because thaw-limited erosion is highly sensitive to water temperature, whereas entrainment-limited erosion is not. Interestingly, the buffered regime produces a thawed layer and relatively slow erosion rates like the entrainment-limited regime, but erosion rates are temperature sensitive like the thaw-limited regime. The results suggest the potential for accelerating erosion in a warming Arctic where bank erosion is presently thaw-limited or buffered. Moreover, rivers can experience all regimes annually and transition between regimes with warming, altering their sensitivity to climate change.

Plain Language Summary

Large river systems flow through regions containing permafrost (permanently frozen ground), which stabilizes riverbanks. As the climate warms, Arctic riverbank erosion processes and rates might change, threatening the homes and livelihoods of communities living along permafrost rivers. Previous work determined that permafrost riverbank erosion can be limited by rates of permafrost thaw or sediment entrainment, whichever process is slower, but did not track heat transfer within the riverbank or the development of a layer of thawed sediment on the bank surface that can insulate permafrost. To address this knowledge gap, we developed a simplified numerical model for permafrost thaw, thawed sediment entrainment, and heat transfer within the thawed and frozen portions of the riverbank. We found that banks form thin layers of thawed sediment, which insulated permafrost and dramatically slowed thaw and erosion rates. For the case where the thawed sediment was unstable and failed past a threshold thickness, the thawed layer remained thin and bank erosion was sensitive to water temperature. Therefore, Arctic rivers may experience higher bank erosion rates as river water warms with climate change in locations where bank erosion occurs under thaw-limited conditions or due to periodic thawed sediment failure for a portion of the year.

1. Introduction

The Arctic contains major river systems that supply 10% of riverine water to Earth's oceans (Peterson et al., 2002; Whitefield et al., 2015) and flow through catchments underlain by permafrost (Obu et al., 2019). Permafrost can dramatically strengthen riverbanks since frozen sand-ice mixtures have tensile strengths of approximately 0.5–1 MPa (Akagawa & Nishisato, 2009; Lange & Ahrens, 1983; Litwin et al., 2012), similar to sandstone bedrock (Sklar & Dietrich, 2001). This strength has led to the idea that melting pore ice is the rate-limiting step in permafrost riverbank erosion (Costard et al., 2003; Lafrenière & Lamoureux, 2019). If Arctic riverbank erosion is thaw-limited, it has broad implications as the climate warms because bank erosion rates are predicted to be highly temperature sensitive (Costard et al., 2003; Lininger & Wohl, 2019). In turn, bank erosion can liberate permafrost carbon, potentially resulting in a positive climate feedback (Douglas et al., 2022; Kanevskiy et al., 2016; Turetsky et al., 2020). Bank erosion also threatens communities and infrastructure in the Arctic (Hjort et al., 2018; Karjalainen et al., 2019; UAF & USACE, 2019), and disproportionately affects the livelihoods of Indigenous communities (Bronen, 2013; Cozzetto et al., 2014).

Thaw-limited bank erosion models make an important assumption: sediment is entrained by the river as soon as it has thawed, therefore continually and directly exposing the pore-ice front to warm, turbulent river water (Costard et al., 2003; Randriamazaoro et al., 2007). Under this scenario, the rate of bank erosion depends on the heat flux from the river water to the frozen bank, with warmer water and higher flow velocities causing more efficient heat transfer into the bank (Costard et al., 2003; Sidorchuk, 1999). Bank erosion rates also depend on the heat required to warm and melt pore ice, which is primarily a function of the volume of pore ice present in the bank (Dupeyrat et al., 2011). Despite these important theoretical advances, existing models appear to substantially overpredict bank erosion rates, drawing into question their validity in forecasting landscape-change scenarios. While rates of several meters per day are possible over limited spatial and temporal scales (Costard et al., 2014; Gautier et al., 2021), thaw-limited models predict rates that are too large by a factor of 10^2 to 10^3 when applied over an entire melt season (Douglas, Miller, et al., 2023; Douglas, Dunne, & Lamb, 2023). This discordance between observation and theory suggests that another process beyond pore-ice melt must limit riverbank erosion rates in permafrost regions (Debol'skaya & Ivanov, 2020; Shur et al., 2021).

One possibility is that erosion rates are limited by sediment entrainment rather than thaw (Costard et al., 2014; Douglas, Miller, et al., 2023; Douglas, Dunne, & Lamb, 2023; Gautier et al., 2021). This aligns with field observations of a layer of thawed sediment tens of cm thick formed on eroding riverbanks on the North Slope of Alaska (Scott, 1978). This layer contradicts a key assumption in the thaw-limited model and indicates that bank erosion could have been limited by the rate of entrainment of thawed sediment from the bank, rather than by the rate of permafrost thaw (Douglas, Miller, et al., 2023; Douglas, Dunne, & Lamb, 2023). Other studies also documented rivers switching from thaw- to entrainment-limited erosion, such as a bluff along the Itkilik River, which eroded very rapidly until it built up a protective apron of sediment (Kanevskiy et al., 2016; Shur et al., 2021). Conceptual models developed based on these observations include multiple stages of bank thaw, collapse, and sediment entrainment (Shur et al., 2021; Tananaev, 2016). Developing a numerical model for this process requires tracking two moving boundaries: the permafrost thaw front and the eroding riverbank. Thus, modeling the thawed layer in permafrost riverbanks poses a distinct challenge that is not fully addressed by models focused on coastal erosion (e.g., Barnhart et al., 2014; Kobayashi & Aktan, 1986), river flooding (Zhang et al., 2023; Zheng et al., 2019), or talik development (Ohara et al., 2022; Roux et al., 2017). Likewise, Douglas, Miller, et al. (2023) and Douglas, Dunne, and Lamb (2023) modeled permafrost riverbank erosion for the thaw- and entrainment-limited end members, but the model is incomplete because they did not dynamically track the pore-ice front nor the thawed-layer development.

Here, we present a numerical model to dynamically track the melting pore-ice front and sediment entrainment from the riverbank surface to create a dynamic thawed layer. First, we present a conceptual model motivated by field observations (Section 2), followed by the mathematical derivation in Section 3. In Section 4, we discuss model implementation and a compilation of observations from Arctic rivers. We show results in Section 5, including controls on thawed layer thickness and how the layer influences erosion mechanics. Finally, we present empiricisms for thaw layer thickness and discuss implications for understanding Arctic riverbank erosion (Section 6).

2. Conceptual Model

2.1. Field Observations

To motivate the formulation of our conceptual model, we first report field observations of thawed layer thickness (Figure 1). Scott (1978) found that noncohesive channel bed and bank material typically formed thawed layers 0–70 cm thick, except at the channel thalweg and apices of thermoerosional niches, where no thawed layer was present (Figures 1a and 1b). In contrast, cohesive bed and bank material formed thawed layers less than 20 cm thick, except in places where erosion was keeping pace with thaw (at the apexes of thermoerosional niches). From May to mid-June, submerged coarser sediment formed a thicker thawed layer than submerged silt, and banks exposed to air had slightly higher (~20%) thicker thawed layers than submerged channel banks and bed.

Figure 1 also shows measurements we made using a permafrost probe of the thickness of the thawed layer exposed to air in June and September 2022 along the Koyukuk River near Huslia, AK (Douglas, Blankenship, et al., 2023). The thawed layer had significant variation in its thickness early in the thaw season and then had a uniform thickness of ~50 cm in the fall (Figure 1d). At the start of the season, the active layer on the neighboring

21699011, 2024, 4, Downloaded from https://agupubs.onlinelibrary.wiley.com/doi/10.1029/2023JF007452 by California Inst of Technology, Wiley Online Library on [14/06/2024]. See the Terms and Conditions (https://onlinelibrary.wiley.com/terms-and-conditions) on Wiley Online Library for rules of use; OA articles are governed by the applicable Creative Commons License

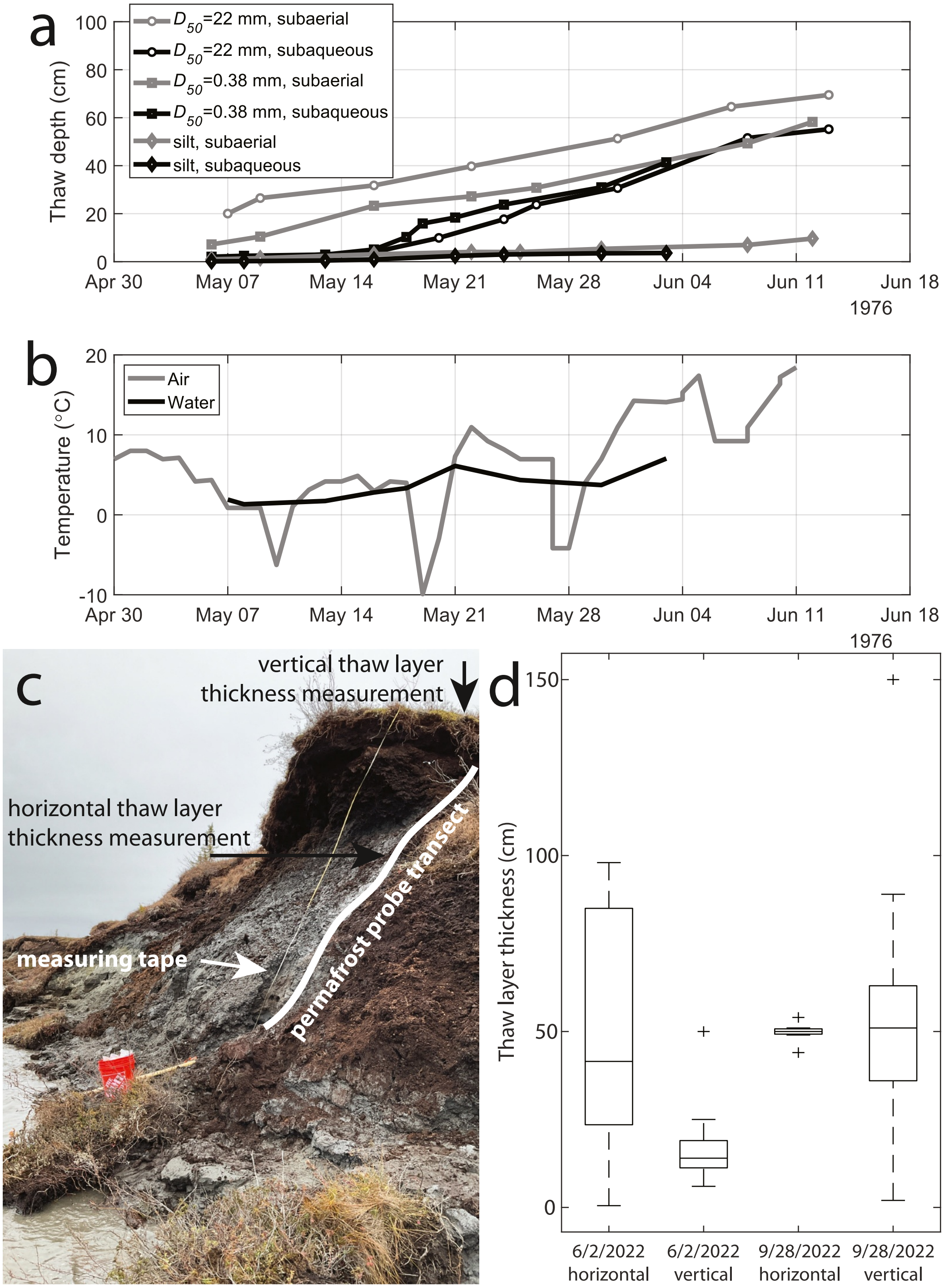

Figure 1. Field examples of thawed layer thickness from permafrost riverbanks along the Atigun and Koyukuk Rivers, AK. (a) Subaerial (gray) and subaqueous (black) measurements of early season thawed layer thickness along the Atigun River by Scott (1978). (b) River water and air temperatures for the Atigun River in summer 1976. (c) Site of horizontal (distance into the riverbank) and vertical (downwards from the top of the floodplain) thawed layer thickness measurements. Measurements were taken on a ~6 m tall bank located at 65.70167°N and 156.3942°W near the village of Huslia, AK. Photograph was taken 9/28/2022 by A. Joshua West. (d) Measurements of horizontal and vertical thawed layer thickness at the site in (c) on 6/2/2022 and 9/28/2022.

21699011, 2024, 4, Downloaded from https://agupubs.onlinelibrary.wiley.com/doi/10.1029/2023JF007452 by California Inst of Technology, Wiley Online Library on [14/06/2024]. See the Terms and Conditions (https://onlinelibrary.wiley.com/terms-and-conditions) on Wiley Online Library for rules of use; OA articles are governed by the applicable Creative Commons License

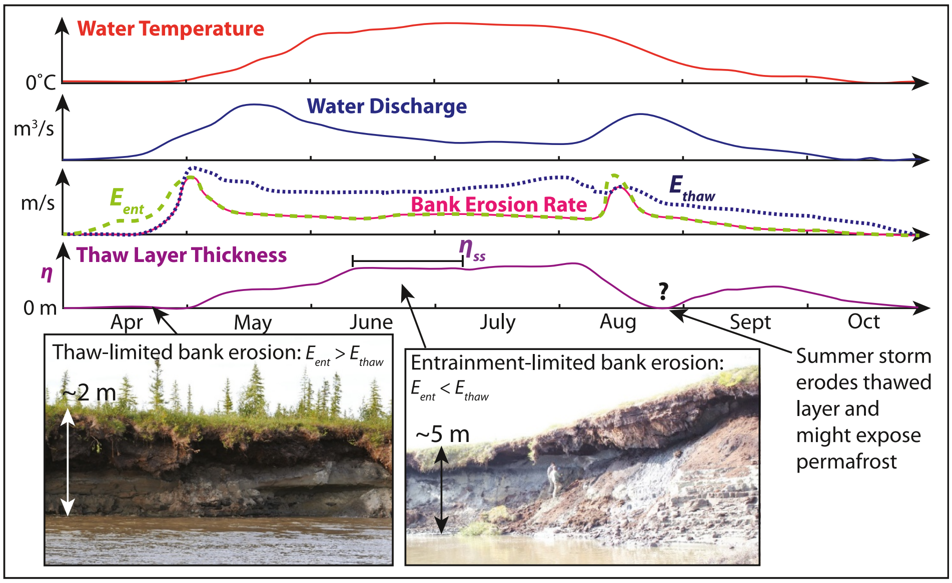

Figure 2. Schematics of water temperature (red curve) and discharge (blue curve) characteristics of Arctic rivers and the resulting riverbank erosion rates (pink curve). Total erosion rates (pink curve) are the minimum of entrainment- and thaw-limited erosion rates (E_{ent}; green dashed curve) and thaw-limited erosion rates (E_{thaw}; blue dashed curve). The thaw layer thickness (η; purple curve) is set by the difference of E_{ent} and E_{thaw} but could approach a constant value (η_{ss}) during periods of steady water temperature and discharge. Annotation of our hypothesized thaw layer thickness plot shows thaw- and entrainment-limited erosion using field photos taken along the Koyukuk River near Huslia, Alaska.

floodplain was much thinner than the thawed layer on the bank, but they reached a similar median thaw depth by the fall. This indicates that the thaw occurred much more quickly laterally on exposed banks than top-down in the floodplain. During summer, the bank' thawed layer did not significantly change its thickness and converged to a value similar to that of the floodplain (Figure 1d).

Taken together, these observations indicate that permafrost riverbanks can have a layer of thawed sediment between river water and permafrost in the riverbank. This thawed layer is typically decimeters thick and tends to be thicker in late summer when water and air temperatures are warm and river discharge is low. Thawed layer thickness and formation rate also appear to increase for riverbanks composed of larger grains. In addition, the presence of this thawed layer indicates that bank erosion likely transitions between thaw- and entrainment-limited styles of erosion.

2.2. Effect of Thaw Layer on Riverbank Erosion

Motivated by these observations of thawed-layer dynamics, we explore the idea that the thawed layer plays an important role in modulating bank erosion rates by considering erosion patterns for an area of the riverbank that remains submerged throughout the year. For instance, as shown in a hypothetical schematic (Figure 2), in the spring, Arctic rivers commonly have high discharge and cold water temperatures. If the sediment entrainment rate from the bank (E_{ent}; m/s) is persistently higher than the pore ice thaw rate (E_{thaw}; m/s), sediment should be swept from the riverbank as soon as it thaws, and a thawed layer should not form. In this case, the rate of bank erosion is thaw-limited and governed by the rate of heat transfer from the turbulent river to the pore-ice and the heat needed to warm and melt the pore ice (Randriamazaoro et al., 2007), and these rates are approximately linearly proportional to water temperature and flow velocity (Costard et al., 2003; Douglas, Dunne, & Lamb, 2023).

By mid-summer, Arctic rivers commonly have a period of warm, low flows (Brabets & Walvoord, 2009; Holmes et al., 2012), which may promote the development of a thawed layer on the bank. The thawed layer grows in thickness (η; m) when the permafrost thaw rate (E_{thaw}) exceeds the sediment entrainment rate (E_{ent}; Figure 2). The thawed layer thickness may reach a dynamic steady state, $\eta = \eta_{ss}$, since the thawed layer buffers heat transfer between permafrost and the flowing water, which can slow thaw rates (Dupeyrat et al., 2011; Roux et al., 2017).

21699011, 2024, 4, Downloaded from https://agupubs.onlinelibrary.wiley.com/doi/10.1029/2023JF007452 by California Inst of Technology, Wiley Online Library on [14/06/2024]. See the Terms and Conditions (https://onlinelibrary.wiley.com/terms-and-conditions) on Wiley Online Library for rules of use; OA articles are governed by the applicable Creative Commons License

21699011, 2024, 4, Downloaded from https://agupubs.onlinelibrary.wiley.com/doi/10.1029/2023JF007452 by California Inst of Technology, Wiley Online Library on [14/06/2024]. See the Terms and Conditions (https://onlinelibrary.wiley.com/terms-and-conditions) on Wiley Online Library for rules of use; OA articles are governed by the applicable Creative Commons License

When a thawed layer is present, bank erosion should be limited by the rate of sediment entrainment and erosion rates should be insensitive to water temperature.

The thawed layer can introduce lags in erosion response during transient changes in forcing. For example, a late season flood might have predicted $E_{\mathrm{ent}} > E_{\mathrm{thaw}}$, which suggests thaw-limited erosion at a steady state. However, bank erosion may still be entrainment-limited until the thaw layer has been eroded completely. Thus, $E_{\mathrm{ent}} > E_{\mathrm{thaw}}$ is a necessary but insufficient condition to produce thaw-limited erosion; in addition, the thaw-layer thickness must be zero (i.e., $\eta = 0$).

An intermediate erosion regime, which we call the buffered regime, might occur if the thawed layer erodes by mass failure (Patsinghasanee et al., 2018; Zhao et al., 2021) rather than by grain-by-grain entrainment. Initially, the thaw layer could be in a state of transient growth where $E_{\mathrm{thaw}} > E_{\mathrm{ent}}$ until a threshold thickness is reached and mass failure occurs. Absent mass failure, the thawed layer would grow to a steady state thickness such that $E_{\mathrm{thaw}} = E_{\mathrm{ent}}$. The rate of bank erosion averaged over many mass failure events would then be set by the rate at which the thawed layer grows, which increases with the difference between E_{ent} and E_{thaw}. Therefore, this regime might be sensitive to the parameters that affect both pore-ice melt and sediment entrainment, including water temperatures, despite the presence of a thawed layer. However, thaw rates will be reduced in comparison to the thaw-limited regime because the thawed layer will thermally buffer the permafrost from the river water (Dupeyrat et al., 2011).

3. Theory Development

In this section, we develop a 1D mathematical framework for a simplified permafrost riverbank erosion that captures the thaw and entrainment processes discussed in our conceptual model. In Section 3.1, we describe the evolution equation for the thaw layer and how to calculate rates of bank sediment entrainment and thaw. In Section 3.2, we describe how heat is transferred through the thawed and frozen regions of the riverbank. Section 3.3 details a nondimensional framework for the bank erosion model and identifies key controlling variables, and Section 3.4 derives an analytical approximation for steady-state thaw layer thickness. All model variables, units, and constants are in Tables S1–S3 in Supporting Information S1.

3.1. Riverbank Thawed Layer Thickness

To determine the thickness of the thawed layer, the model tracks two moving boundaries: the pore ice melting front and the bank erosion front. The evolution of the thawed layer thickness can be found from the mass balance as follows

$$\frac{d\eta}{dt} = E_{\mathrm{ent}} - E_{\mathrm{thaw}}. \tag{1}$$

The permafrost riverbank must be thawed before sediment can be entrained, so $\eta \geq 0$ for all cases.

We calculate the sediment entrainment rate using a common approach (Partheniades, 1965):

$$E_{\mathrm{ent}} = \frac{M(\tau_b/\tau_c - 1)}{(1-\lambda_p)\rho_s}, \tag{2}$$

where τ_b is the fluid shear stress on the bank (Pa), τ_c is the critical shear stress for bank sediment entrainment (Pa), M is a rate coefficient (kg/m^2/s), ρ_s is the density of sediment (we use 2,650 kg/m^3), and λ_p is the dimensionless volumetric porosity. Equation 2 has been used to describe sediment entrainment conditions common in lowland rivers, from cohesive, muddy sediment (Ternat et al., 2008; Winterwerp et al., 2012) to mixtures of cohesionless sand and gravel (e.g., McLean, 1992), and implicitly assumes constant bank material properties.

Following Costard et al. (2003), the rate of permafrost riverbank thaw,

$$E_{\mathrm{thaw}} = \frac{q_w}{\rho_{ic}\left(L_f + c_{p,ic}\left(T_f - T_0\right)\right)}, \tag{3}$$

depends on the heat flux to the bank (q_w; J/m^2/s), the permafrost bulk density (ρ_{ic}; kg/m^3), permafrost latent heat of fusion (L_f; J/kg), the specific heat of the permafrost ($c_{p,ic}$; J/kg/°C), the temperature of fusion for water ice (T_f = 0°C), and the background permafrost temperature (T_0; °C). From mass balance, the bulk density of permafrost (Anisimov et al., 1997),

$$\rho_{ic} = \rho_s(1-\lambda_p) + \rho_{\text{ice}}\lambda_p, \tag{4}$$

depends on the density of water ice (ρ_{ice} = 920 kg/m^3). Following Dupeyrat et al. (2011), we assume that the volumetric pore space is completely filled with ice, so that

$$\lambda_p = \frac{V_{\text{ice}}}{V_{\text{ice}} + V_s}, \tag{5}$$

where V_{ice} is the volume of ice and V_s is the volume of sediment within the bank. For example, permafrost alluvial deposits commonly consist of sediment with its pore space filled with ice or sediment suspended in an ice matrix (Douglas et al., 2022; Lininger et al., 2018). The latent heat of fusion for permafrost (L_f; J/kg) is (Dupeyrat et al., 2011):

$$L_f = \frac{\lambda_p L_{f,\text{ice}}\rho_{\text{ice}}}{\rho_{ic}}, \tag{6}$$

where the latent fusion of ice ($L_{f,\text{ice}}$) is 333,550 J/kg. The specific heat of the sediment-ice mixture ($c_{p,ic}$; J/kg/°C) is (Dupeyrat et al., 2011):

$$c_{p,ic} = \frac{c_{p,\text{ice}}\rho_{\text{ice}}}{\rho_{ic}} + \frac{c_{p,s}\rho_s}{\rho_{ic}}, \tag{7}$$

with the specific heat of ice, $c_{p,\text{ice}}$ = 2093 J/kg/°C, and the specific heat of quartz sand, $c_{p,s}$ = 730 J/kg/°C.

Heat flux from the turbulent river water to the bank (Kader & Yaglom, 1972),

$$q_w = c_{p,w}\rho U C_h (T_w - T_b), \tag{8}$$

is a function of water specific heat ($c_{p,w}$ = 4.184 J/kg/°C), water density (ρ = 1,000 kg/m^3), average downstream water velocity (U; m/s), a heat transfer coefficient (C_h; dimensionless), and the difference in temperature between the water (T_w; °C) and sediment at the bank surface (T_b; °C). For cases where permafrost is directly in contact with the flowing river ($\eta = 0$), $T_b = T_f$, but T_b may exceed 0°C for cases when a layer of thawed sediment develops on the bank. Heat lost by thawing the riverbank is typically not significant compared to the latent heat of total river discharge, so we assume that T_w is not a function of heat transferred to the riverbank (q_w).

We use a heat transfer coefficient, C_h, from Yaglom and Kader (1974) that has performed well compared to numerical experiments (Kuwata, 2021), natural environments (McPhee, 1992), and frozen riverbank-erosion flume experiments (Douglas, Miller, et al., 2023). The parameterization is valid for fully turbulent flow in which the Reynolds number, $Re = UH/\nu > 10^3$, where ν is the fluid kinematic viscosity (m^2/s). The denominator uses an asymptotic match between relations for hydraulically smooth and rough banks:

$$C_h = \frac{\sqrt{C_{f,b}}}{-\alpha \ln \eta_1 + \beta_t + \beta_1}, \tag{9}$$

where $C_{f,b}$ is the wall coefficient of friction (unitless), and empirical constants $\alpha = 2.12$ and $\beta_1 = 0.5$. Equation 9 is a function of roughness element height, $\eta_1 = k_s/H$, where H is the flow depth (m). The coefficient β_t depends on the roughness Reynolds number,

21699011, 2024, 4, Downloaded from https://agupubs.onlinelibrary.wiley.com/doi/10.1029/2023JF007452 by California Inst of Technology, Wiley Online Library on [14/06/2024]. See the Terms and Conditions (https://onlinelibrary.wiley.com/terms-and-conditions) on Wiley Online Library for rules of use; OA articles are governed by the applicable Creative Commons License

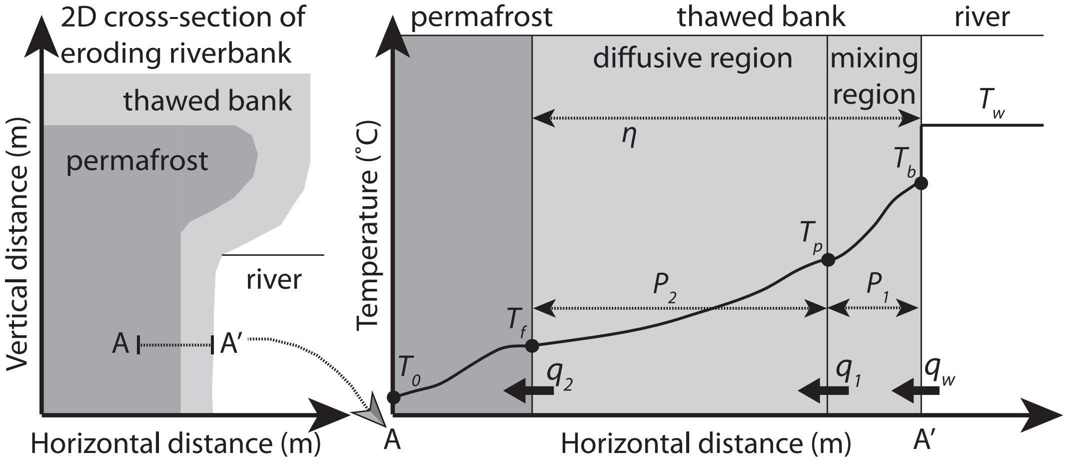

Figure 3. Model region (shown by A-A') in a 2D cross-section of the bank and with a representative temperature profile. Thawed portions of the bank are shown in light gray, permafrost in dark gray, and the river water (flowing into the page) in white. In the modeled 1D transect, the river water has temperature T_w, the bank surface has temperature T_b, the temperature at the boundary between the diffusive and mixing regions is T_p, the temperature at the permafrost thaw front is the fusion temperature for water ice ($T_f = 0°\text{C}$), and permafrost outside the thermal influence of the river has a temperature of T_0. The heat fluxes between each region are q_w, q_1, and q_2, while the thaw layer thickness (η) is equal to the sum of the diffusive (P_2) and mixing region (P_1) thicknesses.

$$Re_{ks} = \frac{k_s u^*}{\nu}, \tag{10}$$

which varies as a function of roughness element height (k_s; m) and near-wall fluid shear velocity (u^*; m/s). We evaluate β_t such that $\beta_t = \beta_r$ for hydraulically rough banks ($Re_{ks} > 100$) and $\beta_t = (Re_{ks}/100)\beta_r + (1 - Re_{ks}/100)\beta_s$ for transitional flow and hydraulically smooth banks ($Re_{ks} \leq 100$). We evaluate the hydraulically rough endmember, $\beta_r = \sqrt{Re_{ks}}\left(b_1\, Pr^{2/3} - b_2\right) + C$, where $C = 9.5$, $b_1 = 0.55$ and $b_2 = 1/11$. The hydraulically smooth endmember is $\beta_s = 12.5Pr^{2/3} - 6$, and in both equations Pr is the dimensionless Prandtl number, a ratio of the kinematic viscosity over the thermal diffusivity of the flowing water.

To model thawed layer failure, we assume for simplicity that the thawed layer de-stabilizes and collapses when it grows beyond a critical thickness, η_{fail} (m). In reality, failure may occur through rotational or translational displacement, and depends on bank geometry and substrate mechanical properties (Patsinghasanee et al., 2018; Zhang et al., 2021; Zhao et al., 2021). We chose a simpler representation because our model is 1D and we assume homogeneous bank mechanical properties.

3.2. Heat Transfer Within Riverbank

We divide the bank material into three regions to model heat transfer: the mixing region, where the flow of river water may cause faster heat transfer via advection through sediment pore space; the diffusive region, consisting of the deeper thawed region with negligible subsurface pore flow; and the frozen permafrost bank material (Figure 3). The presence of a mixing region is consistent with borehole measurements of riverbed thermal diffusivity, which found zones of elevated effective diffusivity tens of cm thick near the surface of cobble-bedded rivers on the Mackenzie River delta (Wankiewicz, 1984).

For scenarios where $\eta > 0$, a layer of thawed sediment insulates permafrost from the flowing river water (Figure 3). Our model must track both bank temperature, since heat flux to and within the bank is a function of temperature, as well as enthalpy, which accounts for the latent heat of fusion (see Section 4.3). We assume that heat is primarily transferred through the bank via conduction (Kudryavtsev et al., 1977; Roux et al., 2017), so

$$\frac{\partial J}{\partial t} = -\kappa \frac{\partial T}{\partial x} A \tag{11}$$

21699011, 2024, 4, Downloaded from https://agupubs.onlinelibrary.wiley.com/doi/10.1029/2023JF007452 by California Inst of Technology, Wiley Online Library on [14/06/2024]. See the Terms and Conditions (https://onlinelibrary.wiley.com/terms-and-conditions) on Wiley Online Library for rules of use; OA articles are governed by the applicable Creative Commons License

where T (°C) is bank temperature, J (J) is enthalpy, κ (J/°C/m/s) is the thermal conductivity, and bank unit area $A = 1$ m^2. This assumption is not valid for coarse sediment with high permeability, where heat fluxes within the bank may be dominated by advection of pore water, or alternatively, the diffusivity must be considered an effective diffusivity that accounts for pore water flow. Similar to previous efforts to model phase change in porous media, we assume that the sediment, pore ice, and water have the same temperature at each location within the bank and calculate bulk thermal diffusivity and conductivity (Beckermann & Viskanta, 1988).

We can convert between bank enthalpy and temperature using riverbank bulk density, thermal conductivity, and specific heat. For permafrost riverbanks, we use Equations 4 and 7, and the thermal conductivity of permafrost (W/m/°C) is:

$$K_{ic} = K_s^{1-\lambda p} K_{\text{ice}}^{\lambda p} \tag{12}$$

This relation uses bank volumetric porosity (λ_p) and the thermal conductivities of water ice ($K_{ice} = 2.18$ W/m/°C) and quartz sand ($K_s = 3.00$ W/m/°C) to evaluate a widely used power-law relation (Slusarchuk & Watson, 1975). Thermal conductivity for the diffusive thawed region is calculated using an analogous equation,

$$K_{ts} = K_s^{1-\lambda p} K_w^{\lambda p} \tag{13}$$

for a constant value of $K_w = 0.606$ W/m/°C. Assuming that the density of the bank does not change significantly upon thaw (Beckermann & Viskanta, 1988; Kudryavtsev et al., 1977), since water and ice have similar densities near freezing, the bulk density of the thawed bank (ρ_{ts}; kg/m^3) is:

$$\rho_{ts} = \rho_s(1 - \lambda_p) + \rho\lambda_p, \tag{14}$$

and the specific heat of thawed permafrost ($c_{p,ts}$; J/kg/°C) is:

$$c_{p,ts} = \frac{c_{p,w}\rho_w}{\rho_{ts}} + \frac{c_{p,s}\rho_s}{\rho_{ts}}. \tag{15}$$

For the outermost mixing region, the flowing river water exerts shear on the pore water within the bank, causing fluid mixing and heat advection into the bank. This region has the same bulk density and specific heat as the diffusive region but has a higher effective thermal conductivity that includes heat advection as well as diffusion. Here, we calculate an effective thermal diffusivity using relations for the mixing region depth, hydraulic conductivity, and subsurface flow which occurs parallel to streamflow that were validated in flume experiments (Lamb et al., 2017). The mixing regime depth for a densely packed porous media (Ghisalberti, 2009) follows

$$P_1 = \frac{2D_{50}}{9C_D(1 - \lambda_p)} \tag{16}$$

and scales with the bank roughness element height (we use the median bank grain size so $k_s = D_{50}$), the bank porosity, and a drag coefficient ($C_D = 1$ for granular beds) (Ghisalberti, 2009). Accounting for dispersion from drag and turbulence within pores (Hsu & Cheng, 1990) is the effective thermal conductivity,

$$K_{\text{eff}} = K_w D_t U_{\text{sub}} \frac{D_{50}}{\alpha_w} \tag{17}$$

and depends on the conductivity of water ($K_w = 0.606$ W/m/°C), an experimental constant ($D_t = 0.12$), the mean subsurface flow velocity (U_{sub}; m/s), the bank median grain size (D_{50}; m), and the thermal diffusivity of water ($\alpha_w = 1.32 \times 10^{-7}$ m^2/s). Since we expect that the mixing region will primarily occur in coarse-grained riverbanks, the subsurface flow is likely non-Darcian. Therefore, we calculate the mean subsurface flow velocity using a modified Forchheimer equation for layer-averaged flow (Lamb et al., 2017):

21699011, 2024, 4, Downloaded from https://agupubs.onlinelibrary.wiley.com/doi/10.1029/2023JF007452 by California Inst of Technology, Wiley Online Library on [14/06/2024]. See the Terms and Conditions (https://onlinelibrary.wiley.com/terms-and-conditions) on Wiley Online Library for rules of use; OA articles are governed by the applicable Creative Commons License

$$U_{\mathrm{sub}} = \frac{1}{2}\sqrt{\left(\frac{1}{C_1 K F^*}\right)^2 + \frac{4S}{C_1\, F^*}\left(\frac{H}{P_1}+1\right)} - \frac{1}{2}\frac{1}{C_1 K F^*}, \tag{18}$$

which depends on the channel slope (S; unitless), the hydraulic conductivity (K; m/m), the thickness of the mixing region (P_1; Equation 16), the nondimensional Forchheimer parameter (F^*), and empirical coefficients. Following Lamb et al. (2017), we take $C_1 = 2$ assuming that negligible pore water flow occurs past the outer mixing layer. We evaluate the nondimensional Forchheimer parameter,

$$F^* = \frac{F\lambda_p}{g\sqrt{K}}, \tag{19}$$

using the Forchheimer coefficient ($F = 5 \times 10^{-3}$; Lamb et al., 2017) and the hydraulic conductivity,

$$K = \frac{k\mu}{\rho g}, \tag{20}$$

which varies with water dynamic viscosity ($\mu = 0.0015$ kg/m/s) and bank hydraulic permeability (k; m^2). Compilations of hydraulic permeability (Barree & Conway, 2004; Bear, 1972; Lapotre & Lamb, 2018; Shepherd, 1989) found good fits to alluvial deposits where

$$k = \frac{a_b \nu}{g(1+Re_b)} D_{50}^{b_b} \tag{21}$$

and the Reynolds number for the pore space is (Barree & Conway, 2004):

$$Re_b = \frac{2U_{\mathrm{sub}} D_{50}}{\nu}. \tag{22}$$

Since a wide range of experimental hydraulic conductivities are observed for a given grain size, we took the mean value of the functions proposed by Lapotre and Lamb (2018) to bound the maximum ($a_b = 6{,}695$ and $b_b = 1.85$) and the minimum ($a_b = 11.9$ and $b_b = 1.5$) for a given grain size and fluid flow characteristics.

3.3. Nondimensionalization of Bank Erosion Model

To compare across scales, we developed a nondimensional version of the model. We nondimensionalize the sediment entrainment rate as

$$E^*_{\mathrm{ent}} = \frac{E_{\mathrm{ent}}}{\sqrt{RgD_{50}}}, \tag{23}$$

where the sediment submerged specific gravity (R) depends on the density of sediment ($\rho_s = 2{,}650$ kg/m^3) and density of water ($\rho = 1{,}000$ kg/m^3) as $R = \rho_s/\rho - 1 = 1.65$.

We nondimensionalize E_{thaw} using the independent variables in Equation 3. Permafrost temperature is nondimensionalized as $T_0^* = T_0 c_{p,ic}/L_f$, and the nondimensional temperature of fusion is similarly $T_f^* = T_f c_{p,ic}/L_f$. Substituting these variables into Equations 3 and 8 produces

$$E^*_{\mathrm{thaw}} = \frac{\rho_{ic} L_f E_{\mathrm{thaw}}}{q_w} = \frac{1}{1 + T_f^* - T_0^*}. \tag{24}$$

Here, $E^*_{\mathrm{thaw}} = 1$ when the permafrost is at its thawing point and the thaw rate is determined by the latent heat of fusion alone. In terrestrial permafrost environments, T_f is very close to 0°C so $T_f^* = 0$. In addition, $c_{p,ic}$ is two orders of magnitude less than L_f, so E^*_{thaw} is usually close to 1.

21699011, 2024, 4, Downloaded from https://agupubs.onlinelibrary.wiley.com/doi/10.1029/2023JF007452 by California Inst of Technology, Wiley Online Library on [14/06/2024]. See the Terms and Conditions (https://onlinelibrary.wiley.com/terms-and-conditions) on Wiley Online Library for rules of use; OA articles are governed by the applicable Creative Commons License

Substituting Equations 23 and 24 into Equation 1 results in a nondimensional governing equation for permafrost riverbank erosion:

$$\frac{d\eta^*}{dt^*} = q^* E^*_{\text{thaw}} - E^*_{\text{ent}}. \tag{25}$$

Here, $\eta^* = \eta / D_{50}$ and $t^* = t\sqrt{D_{50}/Rg}$. The parameter q^* quantifies the relative rates of pore-ice melting at the permafrost thaw front versus sediment entrainment from the bank surface, such that

$$q^* = \left(\frac{q_2}{\rho_{ic} L_f}\right)\left(\frac{1}{\sqrt{RgD_{50}}}\right). \tag{26}$$

Therefore, when $q^* < 1$ the time required to thaw the bank is longer than the time required to erode it, and vice versa when $q^* > 1$. For the case when the bank is at steady-state and the thaw layer thickness is not changing in time, $E^*_{\text{thaw}} \sim 1$ and $q^* \sim E^*_{\text{ent}}$.

3.4. Steady-State Bank Erosion Model

In this section, we derive a steady-state approximation for η^* when the permafrost thaw rate equals the sediment entrainment rate from the surface of the bank. The trivial solution, when $E^*_{\text{ent}} = E^*_{\text{thaw}} = 0$, occurs when the river is frozen over, so $T_w^* = T_w c_{p,ic}/L_f = 0$ and $\eta^* = 0$. For the case when $\frac{d\eta^*}{dt^*} = 0$, the model predicts a dynamic steady state with constant thaw layer thickness ($\eta_{ss}^* = \eta_{ss}/D_{50}$) and

$$E^*_{\text{ent}} = q^* E^*_{\text{thaw}}. \tag{27}$$

Developing an analytical approximation for the steady-state thaw layer thickness requires further constraints and assumptions, so we define the variable $\eta_{ss,a}^* = \eta_{ss,a}/D_{50}$ to represent a simplified, nondimensionalized steady-state thaw layer thickness. Since the mixing region, P_1, is typically much thinner than the diffusive region, P_2 (Figure 3), we assume that $\eta_{ss,a} \sim P_2$. To derive P_2, we assume that the temperature gradient with respect to distance from the riverbank is constant through time and that the heat flux within the bank can be approximated as linear conduction. Thus, for the steady state case, heat flux through the thermally diffusive region ($q_{2,ss}$; J/m^2/s) is:

$$q_{2,ss} = \frac{K_{ts}\left(T_{b,ss} - T_f\right)}{\eta_{ss,a}}, \tag{28}$$

with $T_{b,ss}$ (°C) being the bank temperature exposed to the water (Figure 3).

At steady state, the mixing region must maintain a constant heat flux to the adjacent regions while increasing its temperature to maintain a constant thermal profile as the bank is eroded. Therefore, the heat flux into the bank at steady state ($q_{b,ss}$; J/m^2/s) equals

$$q_{b,ss} = q_{2,ss} + E_{\text{ent}} c_{p,ts} \rho_{ts} \left(T_{b,ss} - T_f\right). \tag{29}$$

Re-arranging and substituting Equations 27–29 with the sediment entrainment rate (Equation 2), heat transfer to the bank (Equation 8), and the erosion rate under thaw-limited conditions (Equation 3) gives an analytical approximation for the thickness of the thawed diffusive region under steady-state conditions:

$$\eta_{ss,a} = \frac{K_{ts}\left(\rho c_{p,w} U C_h \left(T_w - T_f\right) - E_{\text{ent}} \rho_{ic}\left(L_f + c_{p,ic}\left(T_f - T_0\right)\right)\right)}{E_{\text{ent}} \rho_{ic}\left(L_f + c_{p,ic}\left(T_f - T_0\right)\right)\left(\rho c_{p,w} U C_h + \rho_{ts} c_{p,ts} E_{\text{ent}}\right)}. \tag{30}$$

This analytical approximation can be nondimensionalized. We define $U^* = U/\sqrt{RgD_{50}}$, so that the flow velocity scales with the bank sediment settling velocity, and a nondimensional heat transfer coefficient between flowing water and permafrost so that:

21699011, 2024, 4, Downloaded from https://agupubs.onlinelibrary.wiley.com/doi/10.1029/2023JF007452 by California Inst of Technology, Wiley Online Library on [14/06/2024]. See the Terms and Conditions (https://onlinelibrary.wiley.com/terms-and-conditions) on Wiley Online Library for rules of use; OA articles are governed by the applicable Creative Commons License

$$C_h^* = \frac{\rho c_{p,w} C_h}{\rho_{ic} c_{p,ic}}. \tag{31}$$

In addition, we nondimensionalize the ratio of thermal properties for thawed and frozen bank sediment as

$$C_{ic}^* = \frac{\rho_{ic} c_{p,ic}}{\rho_{ts} c_{p,ts}}, \tag{32}$$

and the thermal conductivity for the diffusive region such that

$$K_{ts}^* = \frac{K_{ts}}{\rho_{ts} c_{p,ts}\sqrt{RgD_{50}^3}}. \tag{33}$$

Then, we substitute Equations 31–33 and simplify algebraically to solve for steady-state $\eta_{ss,a}*$. We assume $T_f* = 0$, to produce a simplified equation:

$$\eta_{ss,a}^* \sim \frac{K_{ts}^*\left(C_h^* U^* T_w^* - E_{\text{ent}}^*\left(1 - T_0^*\right)\right)}{E_{\text{ent}}^*\left(1 - T_0^*\right)\left(C_{ic}^* C_h^* U^* + E_{\text{ent}}^*\right)}. \tag{34}$$

In this case, larger values of T_0*, T_w*, and $K*_t$ or smaller values of $C*_{ic}$ and $E_{\text{ent}}*$ will cause a thicker steady-state thaw layer to develop. Equation 34 is valid for the case of a linear temperature profile through the thawed layer, but that is not a necessary condition for steady-state thaw layer thickness. In Section 6.1, we find through comparison to the full model that Equation 34 can also be applied to cases with non-linear temperature profiles using a scaling factor.

4. Data Compilation and Model Implementation

4.1. Arctic Rivers Compilation

To identify appropriate model inputs, we compiled published channel hydraulics, sediment characteristics, and ground thermal properties of permafrost rivers (Text S2, Tables S5 and S6 in Supporting Information S1). The database consists of 27 sites from six rivers with latitudes greater than 62°N and ranging from discontinuous to continuous permafrost regions. We used this data to identify background permafrost temperature (T_0), volumetric porosity (λ_p), bank median grain size (D_{50}), and the water temperature (T_w). We compiled either (1) mean water velocity (U) and depth (H), or (2) the total water discharge (Q_w), channel slope (S), and either the riverbed median grain size ($D_{50,\text{bed}}$) or total coefficient of friction ($C_{f,tot}$). To determine model sensitivity to each parameter, we varied each while holding the others constant. To span the range of values in our compilation, we ran the model for D_{50} from 10^{-5} to 10^{-1} m, λ_p from 0 to 1, T_w from 0 to 20°C, T_0 from -15 to 0°C, and U from 0 to 3 m/s (Section 5.2).

4.2. Yukon River Case Study

In order to understand the response of riverbank erosion to seasonal and inter-annual variability, we examined bank erosion in a scenario modeled roughly after the Yukon River between Stevens Village and Beaver, Alaska. Here, the Yukon River flows through discontinuous permafrost and has an anabranching morphology that converges to a single channel at Stevens Village. The average bank erosion rates along this reach are 2–3 m/yr (Rowland et al., 2019).

We computed the median daily water temperature and discharge and then smoothed the medians using a Savitzky-Golay filter. Water temperature was assumed to be 0°C during periods when no measurements were taken due to ice cover. For discharge, we used the daily timeseries for the Yukon River USGS gage 15453500 at Stevens Village, which is available from 1976 to the present. Water depth and velocity were measured periodically at this gage, and we calculated a power-law relation to discharge at the time of measurement to obtain daily H and U for the USGS gage at Stevens Village (see Figure S2 in Supporting Information S1). Water temperature data were only available sporadically from 1970 to 2005 at Stevens Village ($n = 214$), so we combined this data set with

21699011, 2024, 4, Downloaded from https://agupubs.onlinelibrary.wiley.com/doi/10.1029/2023JF007452 by California Inst of Technology, Wiley Online Library on [14/06/2024]. See the Terms and Conditions (https://onlinelibrary.wiley.com/terms-and-conditions) on Wiley Online Library for rules of use; OA articles are governed by the applicable Creative Commons License

daily water temperature measurements from the downstream gage at Pilot Station, Alaska (USGS gage 15565447). To produce a synthetic hydrograph with a late-summer flood ($Q_{w,sf}$), we combined the mean annual discharge (Q_w) and the discharge reflected so that the freshet was in fall ($Q_{w,\text{flip}}$) such that $Q_{w,sf} = Q^2{}_w + Q^2{}_{w,\text{flip}}$. We then normalized $Q_{w,sf}$ to have the same mean annual discharge as Q_w and used the power-law relations (Figure S2 in Supporting Information S1) to obtain daily timeseries of H and U.

Over this reach, the Yukon River flows over a gravel bed ($D_{50,\text{bed}} \sim 10$ mm) with a slope $S = 1.6 \times 10^{-4}$ (Clement, 1999). We modeled a representative sandy permafrost riverbank with $D_{50} = 1$ mm and $T_f = 0°\text{C}$. We used measurement values of $\rho_b = 861$ kg/m^3 and f_{ice} 0.2362, corresponding to $\lambda_p = 0.22$, for mineral soils on the Yukon Flats between Beaver and Stevens Village (Lininger et al., 2019). For the farfield permafrost temperature, we used $T_0 = -1°\text{C}$, determined from 3 m borehole data for Stevens Village (Biskaborn et al., 2015). To run the model with time-varying discharge and water temperature, we kept channel bank and riverbed properties—such as bank and bed porosity, grain size, permafrost temperature, channel width, and channel slope—constant.

4.3. Model Implementation

We solved the model numerically using second-order finite differences in space and time with $dx = 0.01$ m and $dt = 1$ s. We tracked the thaw front, erosion front, enthalpy, and temperature throughout the bank and the fraction of each bank node that was eroded or thawed. For each model run, we evaluated the von Neumann and Courant-Friedrich-Lewy criteria (Charney et al., 1950; Courant et al., 1928) and selected dx and dt such that the results were non-grid size and time spacing dependent.

Model runs began with a riverbank with constant temperature T_0 and a thaw layer thickness of $\eta = 0$, and subsequently evolved with time-varying boundary conditions.

To solve Equation 2 for E_{ent}, we used an erosion coefficient of $M = 2.5 \times 10^{-5}$ m/s, representative for mixtures of sand and silt (Winterwerp et al., 2012). Shear stress on the channel banks is:

$$\tau_b = \rho C_{f,b} U^2. \tag{35}$$

We assumed that bank roughness is due to sediment using the Manning-Strickler equation:

$$\frac{1}{\sqrt{C_{f,b}}} = 8.1\left(\frac{H}{k_s}\right)^{1/6}. \tag{36}$$

We used a roughness height (k_s; m) set at $k_s = 2.5 \times (2.2D_{50})$ (Rickenmann & Recking, 2011). For cases when $Re_p < 100$, we used the relation of Colebrook-White (Colebrook, 1939) to calculate

$$\frac{1}{\sqrt{8C_{f,b}}} = -2.00\, log_{10}\left(\frac{2.51}{Re\sqrt{8C_{f,b}}} + \frac{k_s}{3.70H}\right). \tag{37}$$

This relation uses $Re = UH/\upsilon$ and converges to that of Manning-Strickler for $Re_p \sim 100$. The critical shear stress for entrainment was evaluated as follows (Parker et al., 2003):

$$\tau_c = (\rho_s - \rho)\, gD_{50}\left(0.11Re_p^{-0.6} + 0.03 \times 10^{-7.7Re_p^{-0.6}}\right), \tag{38}$$

with the particle Reynolds number

$$Re_p = \frac{\sqrt{RgD_{50}^3}}{\upsilon}. \tag{39}$$

To evaluate Equation 3 for E_{thaw}, we used H and $C_{f,b}$ to evaluate Equations 9 and 10 for C_h, which was then substituted into Equation 8 to compute the heat transferred from the water to the riverbank. To evaluate

21699011, 2024, 4, Downloaded from https://agupubs.onlinelibrary.wiley.com/doi/10.1029/2023JF007452 by California Inst of Technology, Wiley Online Library on [14/06/2024]. See the Terms and Conditions (https://onlinelibrary.wiley.com/terms-and-conditions) on Wiley Online Library for rules of use; OA articles are governed by the applicable Creative Commons License

Equations 9 and 10, we used $u^* = U\sqrt{C_{f,b}}$ and obtained the flow depth by balancing the depth-slope product with channel bed friction under normal flow conditions:

$$H = \frac{C_{f,tot}U^2}{gS}, \tag{40}$$

with $C_{f,tot}$ (unitless) the total coefficient of friction.

Heat was supplied to the boundary node at the edge of the eroding bank using Equation 3 and diffused through the bank across a fixed grid. At each timestep, we evaluated Equations 4–7 to solve for the material properties (bulk density, specific heat capacity, and thermal conductivity) of the frozen riverbank. For the case when $\eta > 0$ (Figure 3), we used Equations 16–22 to compute the P_1 thickness and material properties and Equations 11–15 for P_2. When $0 < \eta < P_1$ we set the entire thawed-layer thermal conductivity equal to that of the mixing region. For nodes containing the thaw front and boundary between the diffusive and mixing regions, we calculated their material properties according to a linear average weighted by the fraction of the node comprising each layer (Beckermann & Viskanta, 1988). For instance, a node may contain fractions f_a of layer a and f_b of layer b where $f_a + f_b = 1$. After calculating the thermal and material properties throughout the bank, we propagated heat using an upwinding finite difference scheme for thermal diffusion (Equation 11). For the node at the thaw front, heat in excess of 0°C was used to partially thaw that node. After updating the bank temperature and thaw front, we calculated the rate of total riverbank erosion using Equation 2 and updated the erosion front to reflect this new value or the location of the thaw front if all sediment thawed during that timestep would be eroded. All nodes that had been eroded from the riverbank had their temperature and enthalpy set equal to those of the river water. The updated temperature, enthalpy, and locations of the erosion and thaw fronts were used to calculate bank erosion in the next timestep.

We determined when the model reached a steady state when the thawed layer thickness at time t was within a very small difference of its mean value (η_{mean}) calculated over a representative timescale prior to time t (t–t_c). The criterion was $(\eta_{\text{mean}}-\eta)/\eta_{\text{mean}} < 10^{-3}$ and t_c was calculated as $t_c = 100 \times E_{\text{ent}}/(dx/dt)$.

5. Results

In this section, we illustrate the model response to the range of conditions observed in terrestrial permafrost river systems. First, we investigate model transient behavior under idealized constant forcing for the base case scenario as well as related scenarios with different grain size and bank ice content without allowing thaw-layer failure (Section 5.1). Next, we show the numerical model results for steady-state thaw layer thickness by changing parameters from a base case again while not allowing failure (Section 5.2). After exploring model behavior under steady forcing, we ran the model for transient forcing typical of Arctic rivers. Section 5.3 describes experimental results obtained using an annual hydrograph and water temperature curve typical for the Yukon River in Alaska as well as a synthetic hydrograph with a late-summer flood caused by localized rainfall. Then, we investigate the buffered regime for different bank failure thresholds at constant conditions and for the same typical hydrograph (Section 5.4) to evaluate how periodic bank failure changes the sensitivity of erosion rates to water temperature.

5.1. Model Behavior for a Base Case Under Steady Forcing

To illustrate the behavior of the numerical model through time, we ran the model for a base case under steady forcing. The base case, which was based on measurements of the Yukon River and its banks (Table 1), had a moderate water temperature ($T_w = 10$°C), low volumetric ice content ($\lambda_p = 0.22$), and coarse sand banks ($D_{50} = 1$ mm; Figure 4a). This case was entrainment-limited, so that the bank thawed more rapidly than it eroded and a thawed layer formed. The thaw rate was initially rapid since a steep temperature gradient formed in the thawed layer between the bank surface and the thawing permafrost, producing high heat fluxes into the permafrost. As the thaw layer thickened, the temperature at the bank surface increased, decreasing the heat flux into the thawed layer, and the temperature gradient decreased. Together, these effects caused the thaw rate to decline and approached the bank sediment entrainment rate, producing a nearly steady-state thaw layer thickness of 14 cm after 48 hr.

21699011, 2024, 4, Downloaded from https://agupubs.onlinelibrary.wiley.com/doi/10.1029/2023JF007452 by California Inst of Technology, Wiley Online Library on [14/06/2024]. See the Terms and Conditions (https://onlinelibrary.wiley.com/terms-and-conditions) on Wiley Online Library for rules of use; OA articles are governed by the applicable Creative Commons License

Table 1
Numerical Model Input Values for the Base Case of the Yukon River and the Range of Natural Rivers in Our Data Compilation

Model input variables	Symbol	Yukon River (base case)	Compilation range
Bank median grain size	D_{50}	1×10^{-3} m	7.70×10^{-6} to 2.2×10^{-2} m
River water surface slope	S	1.6×10^{-4}	2.71×10^{-5} to 1.6×10^{-3}
Permafrost porosity	λ_p	0.22 m^3/m^3	0–1 m^3/m^3
River water temperature	T_w	10°C	0–20°C
Background permafrost temperature	T_0	−1°C	−6.6 to −0.1°C
Mean river water flow velocity	U	1.0 m/s	0.122–2.04 m/s

To investigate the effects of the pore ice content, we increased λ_p from 0.22 to 0.50 (Figure 4b) and 0.80 (Figure 4c). As the pore ice content increased, the modeled entrainment rate increased, erosion rates remained entrainment-limited, and the thaw layer thickness decreased. The entrainment rate was proportional to $(1\text{-} \lambda_p)^{-1}$ since the river could entrain sediment at a constant volumetric rate, all else being equal, so decreasing the concentration of sediment in the bank increased entrainment rates. Increasing λ_p also produced a thinner thawed layer with 4.7 and 1.2 cm nearly constant thicknesses for $\lambda_p = 0.50$ and 0.80 after the model was run for 48 hr. The steady-state thaw layer thickness decreased because at the same time sediment entrainment becomes more efficient, the higher volume fraction of ice required more heat to thaw the same volume of bank material. Both cases initially thawed rapidly, but the bank with higher porosity reached steady state more rapidly because of the thinner thawed layer. Therefore, for riverbanks with the same hydraulic and thermal conditions, increasing the volume fraction of ice will increase sediment entrainment rates and decrease the rate of pore ice melting.

Next, we ran the model for the base case conditions (Table 1) and changed the bank grain size from sand (D_{50} = 1 mm) to silt (D_{50} = 50 μm) and to gravel (D_{50} = 1 cm). For the frozen silt case (Figure 4d), the bank experienced more rapid sediment entrainment (2.5 cm/day). The sediment entrainment rates were more rapid than the equivalent sandy bank because the entrainment rate depends on the excess shear stress (Equation 2) and τ_c varied as a function of grain size according to the Shields curve (Equations 38 and 39; Parker et al., 2003). Despite more rapid sediment entrainment, the silt bank model run predicted entrainment-limited conditions and produced a thawed layer 17 cm thick after 48 hr (Figure 4d). This thawed layer thickness reflected competition between the rates of bank thaw and sediment entrainment, with initially rapid thaw causing an abrupt increase in thawed layer thickness that gradually slowed as the thawed layer approached a steady-state thickness. Compared to a sand bank with the same ice content (Figure 4a), the silt bank thaw layer was thinner because sediment entrainment was more efficient for the finer grain size. When compared to a sandy bank with similar entrainment rates but higher pore ice content (Figure 4c), the silt bank had a thicker thawed layer because thawing the frozen bank required less heat. Therefore, differences in thawed layer thickness between the silt and sand riverbank cases reflected competition between the efficiency of pore ice melt and the rate of sediment entrainment, which was influenced by the volume of pore ice in the bank as well as the shape of the Shields curve.

For the gravel riverbank case (D_{50} = 1 cm), base case hydraulic conditions were below the threshold of entrainment and erosion was zero (Figures 4e–4g). For the gravel case, and other conditions when $E = 0$, a steady state where bank thaw and erosion occur at the same rate could not occur unless T_w = 0°C, though permafrost thaw rates gradually approached 0 m/s as the thawed layer thickened. Under these conditions, entrainment rates were zero and a thawed layer 20 cm thick developed within 2 days when $\lambda_p = 0.22$ (Figure 4e). This thawed layer was slightly thicker than the one that forms for a sandy bank with equivalent conditions except for grain size (Figure 4a) because thawed sediment was not removed from the bank. However, the thaw front penetrated less deeply into the bank for the immobile gravel when compared to the equivalent silt (Figure 4d) and sand conditions. This result was because the bank surface temperature increased and the temperature gradient decreased as the thaw layer thickened (Figure 4e). Therefore, a combination of rapid sediment entrainment and heat transfer to the riverbanks was required to promote rapid bank erosion.

Next, we increased λ_p–0.5 and 0.8 for the gravel case, keeping all other variables constant (Figures 4e–4g). Similar to the sandy bank (Figures 4a–4c), the thaw layer thickness that formed over 2 days decreased (to 12 then 9 cm) as the pore ice content increased. Sediment entrainment rates remained zero since although the fraction of

21699011, 2024, 4, Downloaded from https://agupubs.onlinelibrary.wiley.com/doi/10.1029/2023JF007452 by California Inst of Technology, Wiley Online Library on [14/06/2024]. See the Terms and Conditions (https://onlinelibrary.wiley.com/terms-and-conditions) on Wiley Online Library for rules of use; OA articles are governed by the applicable Creative Commons License

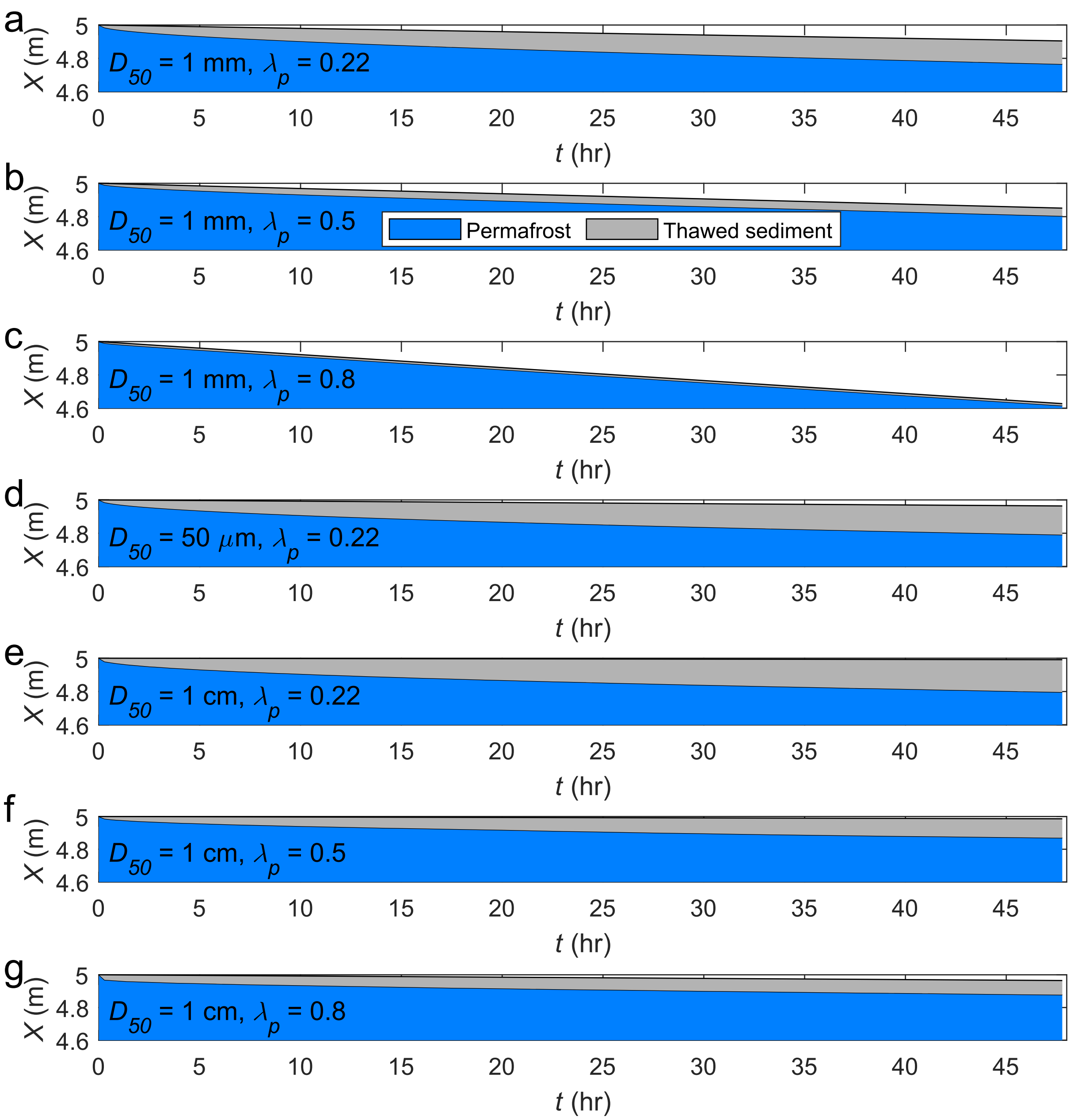

Figure 4. Model results for riverbank thaw and erosion under constant hydraulic conditions. The thawed layer (gray) and permafrost (blue) retreat from their initial position of $X = 5$ m (y-axis) during the 1-hr model run (time on x-axis). The model was run for the Yukon River base case conditions for varying bank grain size (D_{50}) and volumetric porosity (λ_p). Model runs include: (a) $D_{50} = 1$ mm and $\lambda_p = 0.22$, (b) $D_{50} = 1$ mm and $\lambda_p = 0.50$, (c) $D_{50} = 1$ mm, and $\lambda_p = 0.80$, (d) $D_{50} = 50$ μm and $\lambda_p = 0.22$, (e) $D_{50} = 1$ cm and $\lambda_p = 0.22$, (f) $D_{50} = 1$ cm and $\lambda_p = 0.50$, and (g) $D_{50} = 1$ cm and $\lambda_p = 0.80$.

sediment in the bank decreased the stress exerted by near-bank flow was still less than stress required to entrain individual grains of gravel (Figures 4e–4g). Therefore, the decrease in thawed layer thickness was solely due to the increase in heat required to thaw the bank.

Together, the results presented in Figure 4 indicate that steady-state thawed layer thickness generally decreases as volumetric pore ice increases because entrainment rates increase while bank thaw rates decrease. In addition, grain size affected thaw layer thickness by changing the critical shear stress required to entrain sediment via the Shields curve and altering the rate of heat transfer as a function of bank roughness. We explored these trends further in Section 5.2 by systematically varying the main parameters in the model and comparing the resulting steady-state thaw layer thicknesses.

21699011, 2024, 4, Downloaded from https://agupubs.onlinelibrary.wiley.com/doi/10.1029/2023JF007452 by California Inst of Technology, Wiley Online Library on [14/06/2024]. See the Terms and Conditions (https://onlinelibrary.wiley.com/terms-and-conditions) on Wiley Online Library for rules of use; OA articles are governed by the applicable Creative Commons License

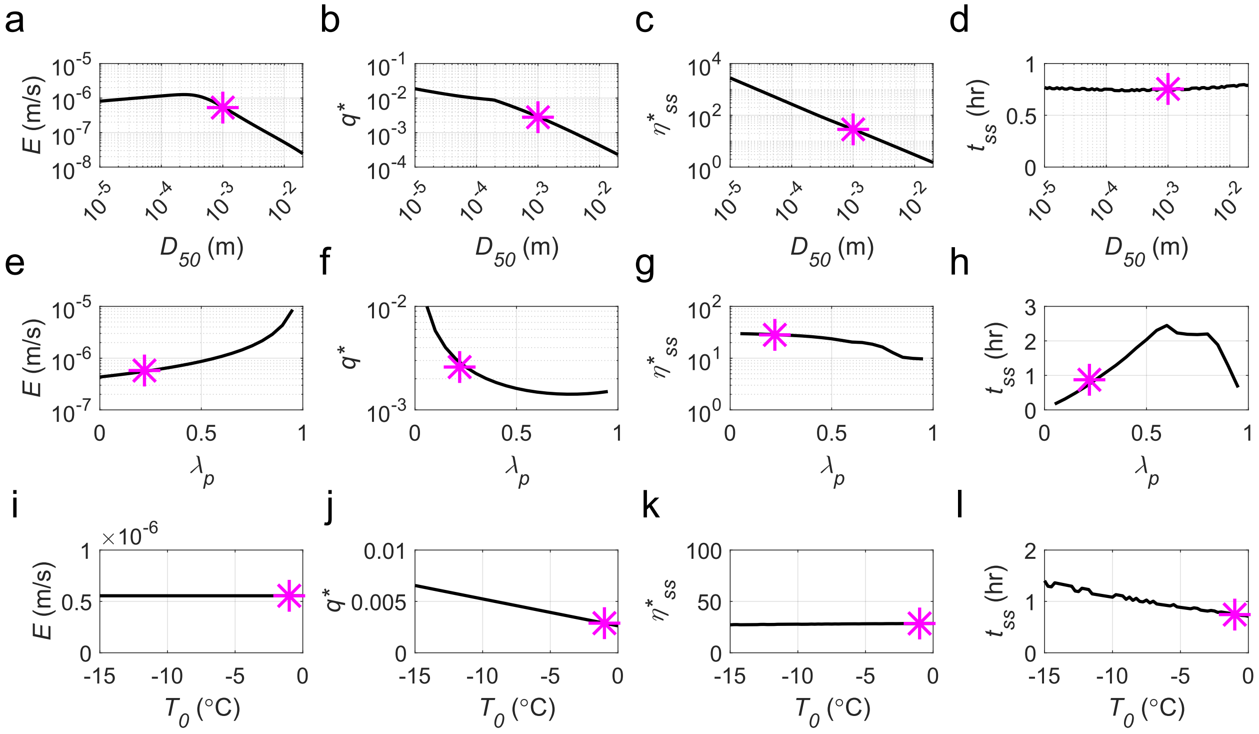

Figure 5. Effect of riverbank properties on riverbank erosion processes, with the base case marked as a pink star on each plot. (a) Riverbank erosion rates versus median grain size (D_{50}). (b) Dimensionless initial heat transfer rate (q_0*) versus D_{50}. (c) Steady-state thickness η_{ss}* versus D_{50}. (d) Timescale to reach steady-state thaw layer thickness (t_{ss}) versus D_{50}. (e) Riverbank erosion rates versus volumetric ice content (λ_p). (f) Dimensionless heat transfer rate (q*) versus λ_p. (g) Steady-state thickness η_{ss}* versus λ_p. (h) Steady-state timescale t_{ss} versus λ_p. (i) Riverbank erosion rates versus permafrost temperature (T_0). (j) Dimensionless heat transfer rate (q*) versus T_0. (k) Steady-state thickness η_{ss}* versus T_0. (l) Steady-state timescale t_{ss} versus T_0.

5.2. Controls on Steady-State Thaw-Layer Thickness

To explore the parameter space of steady thaw layer thickness, we ran the full model to steady state. For each model run, we held all variables constant from our base case (Table 1) and varied one parameter at a time. For each parameter, we plotted the bank erosion rate (E, m/s), dimensionless heat flux at the model run initial conditions (q*), and dimensionless steady-state thaw layer thickness (η^*_{ss}). We used the numerical model instead of the analytical approximation to determine the steady state because all realistic values for implementing the model resulted in a non-linear temperature profile, breaking assumptions in the analytical approximation, which is discussed in more detail in Section 6.1. For each numerical model run, we determined whether bank erosion was entrainment- or thaw-limited based on the presence or absence of a thawed layer as well as the time to reach steady-state conditions. Most model runs reached a steady state within ∼2 hr. Though this timescale will necessarily change depending on the choice of steady-state criteria, we expect that most natural rivers should reach steady-state conditions on approximately a 10-hr timescale for constant or very gradually varied river flow conditions.

First, we varied bank sediment grain size from silt to gravel. All scenarios with varying grain size had entrainment-limited erosion, with permafrost thaw outpacing sediment entrainment (Figure 5). Bank erosion rates were high for small grain sizes, though the entrainment rate decreased steeply with grain size in the fully rough hydraulic regime (Figure 5a). The dimensionless heat flux to the bank (q*) at small grain sizes was orders of magnitude less than 1 and decreased with increasing bank roughness (Figure 5b). The gradient of q* relative to D_{50} is shallow for transitional banks and becomes steeper when banks become rough hydraulically. Coarser banks result in a lower heat flux because increasing bank roughness decreases the coefficient of heat transfer in the hydraulically rough regime due to slower heat advection to the bank in the eddies of bank roughness elements (Yaglom & Kader, 1974). At steady state, this lower heat flux associated with coarser grains resulted in a smaller thaw layer thickness (η^*_{ss}) because less insulation was needed for the thaw rate to equal the erosion rate (Figure 5c). Bank grain size did not affect t_{ss}, which remained approximately 0.75 hr throughout different hydraulic regimes (Figure 5d).

21699011, 2024, 4, Downloaded from https://agupubs.onlinelibrary.wiley.com/doi/10.1029/2023JF007452 by California Inst of Technology, Wiley Online Library on [14/06/2024]. See the Terms and Conditions (https://onlinelibrary.wiley.com/terms-and-conditions) on Wiley Online Library for rules of use; OA articles are governed by the applicable Creative Commons License

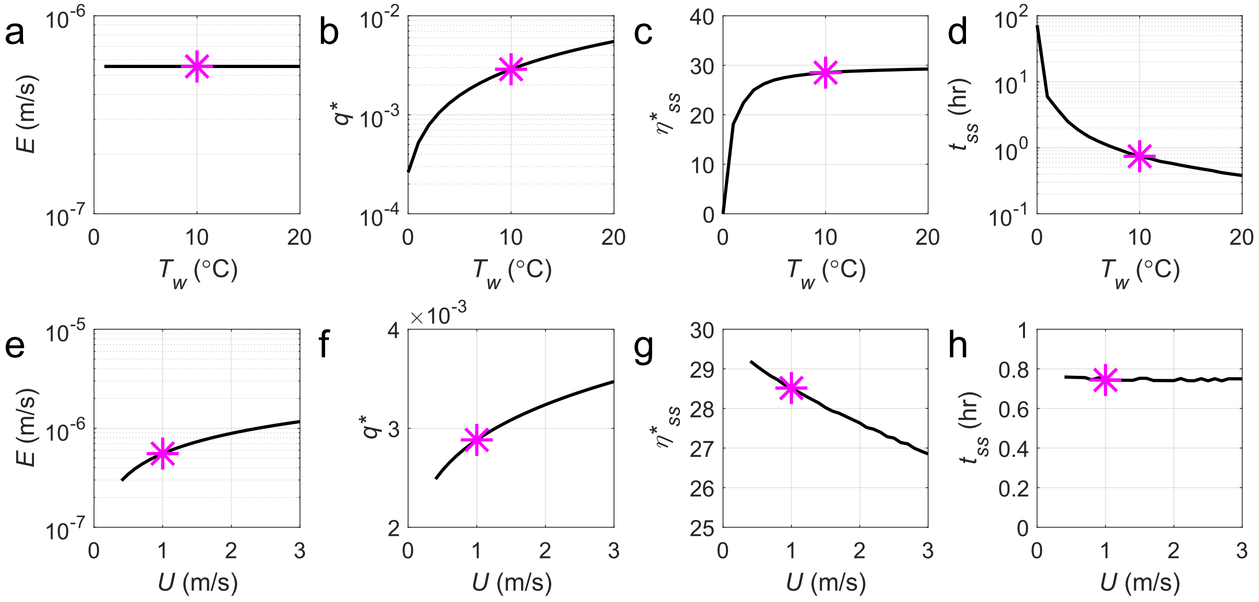

Figure 6. Effect of river properties on riverbank erosion processes with the base case marked as a pink star on each plot. (a) Riverbank erosion rates versus river water temperature (T_w). (b) Dimensionless heat transfer rate (q^*) versus T_w. (c) Steady-state thickness η_{ss}^* versus T_w. (d) Timescale to steady state (t_{ss}) versus T_w. (e) Riverbank erosion rates versus water flow velocity (U). (f) Dimensionless heat transfer rate (q^*) versus U. (g) Steady-state thickness η_{ss}^* versus U. (h) Timescale to steady state (t_{ss}) versus T_w.

Next, we evaluated the sensitivity of modeled riverbank erosion rates to pore ice content (Figures 5e–5h). We ran the model for 0 to 100 vol% pore ice (corresponding to 100 to 0 vol% quartz sand) to span the range of observed permafrost volumetric ice contents (Section 4.1). The bank was entrainment-limited for all cases except $\lambda_p = 1$. At low pore ice contents, there was a high fraction of sand in the bank, so entrainment rates were relatively slow (Figure 5e). As the fraction of sand per unit volume of the bank decreased and the fraction of ice rose, sediment entrainment rates increased proportional to $1/(1-\lambda_p)$, following Equation 2. Increasing λ_p simultaneously decreased permafrost thaw rates due to the higher latent heat of fusion to thaw the bank. Therefore, η_{ss} declined from ~300 to 100 grain diameters as λ_p approached 1 (Figure 5g). For the same change in ice content, the thaw layer thickness decreased by approximately two orders of magnitude while the entrainment rate increased by approximately one order of magnitude. The time to reach the steady state first increased with λ_p as heat fluxes decreased more rapidly than erosion rates increased and then decreased for high λ_p (Figure 5h). Although faster entrainment rates required higher heat fluxes to obtain steady-state conditions, the thermal gradient through the thawed layer increased even more rapidly than entrainment rates, so q^* must have decreased to reach the steady state (Figure 5f). At high ice contents, rising entrainment rates balanced decreasing permafrost thaw rates, causing values of q^* to plateau. Eventually, the entrainment rate must asymptote to infinity as $\lambda_p = 1$, so q^* flattened and then slightly curved upward for $\lambda_p > 0.80$.

Permafrost temperature had little influence on bank erosion or thaw rates and only a slight influence on the thawed layer thickness (Figure 5). Since entrainment rates did not depend on bank temperature when there was a thawed layer present, total bank erosion rates did not vary with permafrost temperature (Figure 5i). Increasing bank temperature reduced the heat required to raise the permafrost to the pore ice melting point at 0°C. As a result, permafrost thaw was marginally more efficient and the thaw layer thickness increased from 27 to 29 grain diameters with increasing bank temperature (Figure 5k). The slight increase in permafrost thaw efficiency caused q^* to decrease as permafrost temperature increased (Figure 5j). However, the permafrost thaw rate and the time to steady state did not significantly change with bank temperature because the latent heat of fusion for water ice is two orders of magnitude higher than the specific heat of ice (Equation 3; Figure 5l).

Since the Yukon River example case was almost always entrainment-limited for $T_w > 0$°C, river water temperature did not have a significant effect on bank erosion rates (Figure 6a). However, increasing T_w raised the heat flux from the river to the bank (Figure 6b) because q^* is linearly proportional to the difference between water and bank surface temperature (Equation 8). Reaching steady-state thaw layer thickness required that permafrost thaw

21699011, 2024, 4, Downloaded from https://agupubs.onlinelibrary.wiley.com/doi/10.1029/2023JF007452 by California Inst of Technology, Wiley Online Library on [14/06/2024]. See the Terms and Conditions (https://onlinelibrary.wiley.com/terms-and-conditions) on Wiley Online Library for rules of use; OA articles are governed by the applicable Creative Commons License

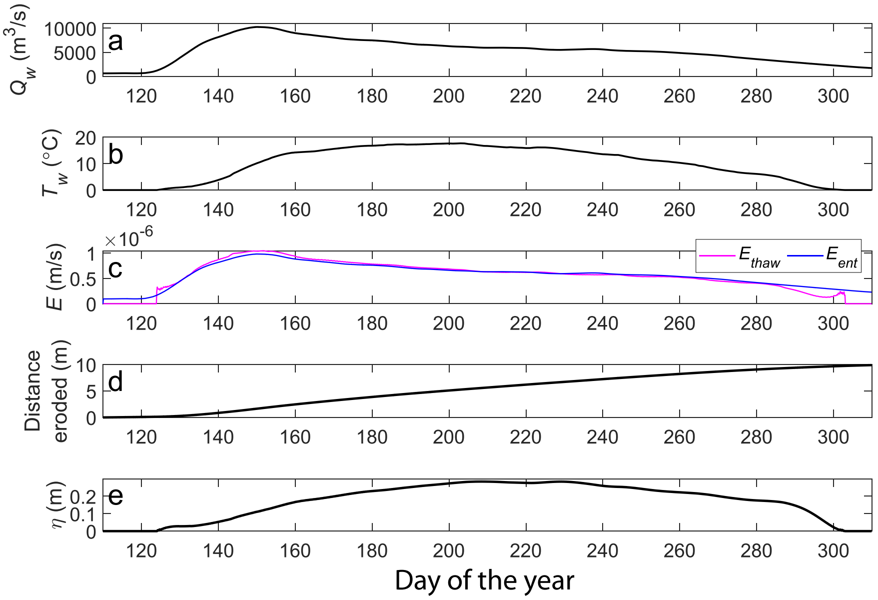

Figure 7. Bank erosion for the Yukon River as a function of discharge and water temperature through its annual hydrograph. (a) Median daily water discharge versus measurement day of the year from the Yukon River USGS stream gage at Stevens Village, Alaska. (b) Median daily water temperature measurements from Stevens Village, which were taken intermittently, combined with daily measurements from Pilot Station. (c) Modeled erosion rates for the modern hydrograph of the Yukon River. (d) Cumulative bank erosion versus day of the year. (e) Modeled thaw layer thickness versus day of the year for the modern hydrograph.

occurred at the same rate as sediment entrainment. Therefore, increasing $q*$ drove the formation of a thicker insulating thaw layer ranging from ~0 to 30 grains thick to equilibrate thaw and entrainment rates (Figure 6c). Thaw layer thickness reached steady state conditions more rapidly with increasing water temperature as t_{ss} decreased to less than an hour (Figure 6d).

Faster water flow velocity increased both thaw and entrainment rates (Equation 3 and 8). Erosion rates formed an increasing concave-down trend with flow velocity because sediment entrainment rates depended linearly on excess shear stress, which scaled roughly as U^2 (Figure 6e). Increasing U also caused an increase in the heat transfer coefficient and heat flux to the bank, which was linearly proportional to the flow velocity (Figure 6f). Since E scaled as U^2 and $q*$ scaled as U, sediment entrainment rates increased more rapidly than thaw rates with greater flow velocity. Therefore, with faster flow velocity, the rate of heat transfer through the thawed layer must have increased more rapidly than the efficiency of heat transfer to the bank, so the insulating thawed layer was thinner (Figure 6g). The thaw layer thickness approached the steady state in ~45 min for all flow velocities able to entrain sediment (Figure 6h).

The trends investigated in this section were apparent for model runs with constant hydraulic and thermal conditions but might not be easily observed for transient hydraulic and thermal conditions, which are explored in Section 5.3.

5.3. Seasonal Variations in Thaw-Layer Thickness

To understand the processes limiting riverbank erosion in time, we ran the model over a typical annual hydrograph for the Yukon River (Figure 7). At the start of the summer, water temperature began near 0°C, peaked midsummer, and then dropped back to zero as the river ices over in the fall (Figure 7b). Water discharge started from zero with complete ice cover and then peaked in the early summer with the spring snowmelt and ice break-up before subsiding to a relatively constant discharge mid-summer and declining in the fall (Figure 7a). Entrainment-limited erosion (when $\eta > 0$) occurred throughout the summer and produced 9.97 m of erosion (Figure 7c). The thawed layer remained relatively thin (<30 cm) throughout the summer but slowed bank thaw rates so that they equaled entrainment-limited erosion rates, producing near steady-state conditions (Figures 7c and e). This was because our results earlier (Sections 5.1 and 5.2) showed that the thawed layer typically took

21699011, 2024, 4, Downloaded from https://agupubs.onlinelibrary.wiley.com/doi/10.1029/2023JF007452 by California Inst of Technology, Wiley Online Library on [14/06/2024]. See the Terms and Conditions (https://onlinelibrary.wiley.com/terms-and-conditions) on Wiley Online Library for rules of use; OA articles are governed by the applicable Creative Commons License

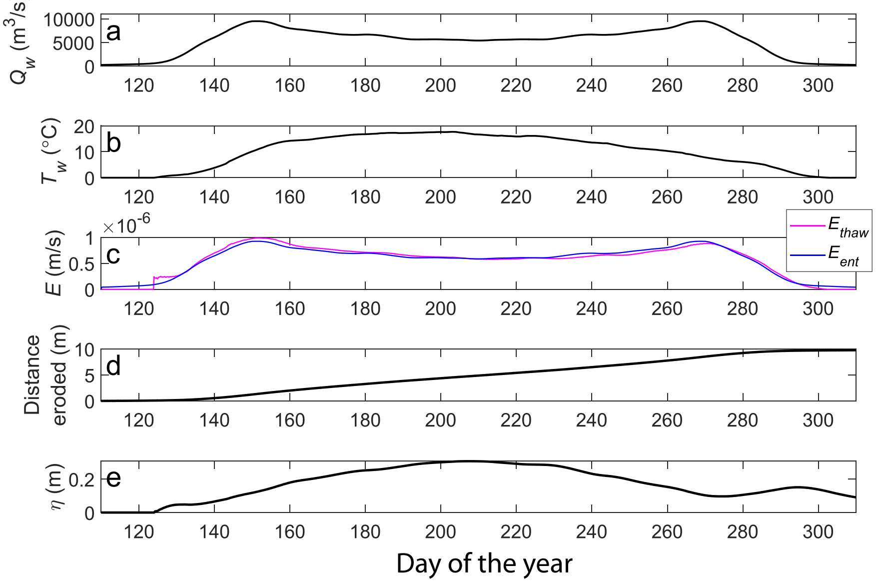

Figure 8. Bank erosion for the Yukon River as a function of discharge and water temperature, with a synthetic hydrograph so discharge peaks in early and late summer. (a) Synthetic daily water discharge versus measurement day of the year for the Yukon River. (b) Median daily water temperature measurements from Stevens Village, which were taken intermittently, combined with measurements from Pilot Station. (c) Modeled erosion rates for the synthetic hydrograph of the Yukon River. (d) Cumulative bank erosion versus day of the year. (e) Modeled thaw layer thickness versus day of the year.

hours to reach a steady state, while the river hydrograph (Figures 7a and 7b) changed over the course of days throughout the summer. Permafrost thaw rates remained slightly higher than E_{ent} during the early portions of the thaw season when water temperatures were warming, and were slightly lower than E_{ent} in the late summer when water temperatures were colder. Therefore, although conditions remained near a steady state for most of the summer, there was a slight tendency to thicken the thawed layer early in the summer and decrease the thawed layer thickness toward the end of summer. Importantly, the thawed layer prevented thaw-limited conditions in fall when water temperatures and discharges declined, which occurred after day 280 in Figure 7c. At the end of summer, the entrainment rate was faster than the permafrost thaw rate; however, there was still a thawed layer present on the bank, so erosion was still limited by sediment entrainment. Therefore, conditions where entrainment rates exceed thaw rates must persist long enough to reach $\eta = 0$ before bank erosion switches from the entrainment- to thaw-limited erosion regime.

To investigate whether bank erosion rates and processes varied in response to late-summer floods, we ran the model using the same parameters and the same average annual discharge as in Figure 7, but we changed the shape of the hydrograph to include a late season flood (Section 4.2; Figure 8a). Model results indicated that bank erosion was sediment entrainment-limited throughout the summer and fall, similar to model results without the late-summer flood (Figure 8c). Results indicated 9.87 m of erosion during the summer months, a decrease of 10 cm compared to the case without a summer flood. The slight decrease in net erosion occurred because sediment entrainment was non-linearly related to flow velocity, and by including the late summer flood, we partitioned the mean discharge between two floods rather than one, resulting in lower peak flow rates and shear stresses. The thawed layer developed during the spring flood and then gradually thinned and disappeared throughout the summer (Figure 8e). Similar to the results for the typical modern hydrograph, the thawed layer remained in a quasi-steady state throughout the summer, such that E_{ent} was slightly less than E_{thaw} in early summer and slightly greater than E_{thaw} in late summer (Figure 8c). The primary exception to the quasi-steady state was when water temperatures first exceeded 0°C around day 125, which caused a rapid thaw back of the bank to form the initial thawed layer. As this layer thickened, E_{thaw} briefly spiked since rising water temperatures triggered rapid permafrost degradation before slowly declining to match E_{ent}.

The result that late-summer floods did not produce thaw-limited conditions was seemingly counter-intuitive, as we hypothesized that a late-summer flood should rapidly entrain sediment and expose permafrost (Figure 2).

21699011, 2024, 4, Downloaded from https://agupubs.onlinelibrary.wiley.com/doi/10.1029/2023JF007452 by California Inst of Technology, Wiley Online Library on [14/06/2024]. See the Terms and Conditions (https://onlinelibrary.wiley.com/terms-and-conditions) on Wiley Online Library for rules of use; OA articles are governed by the applicable Creative Commons License

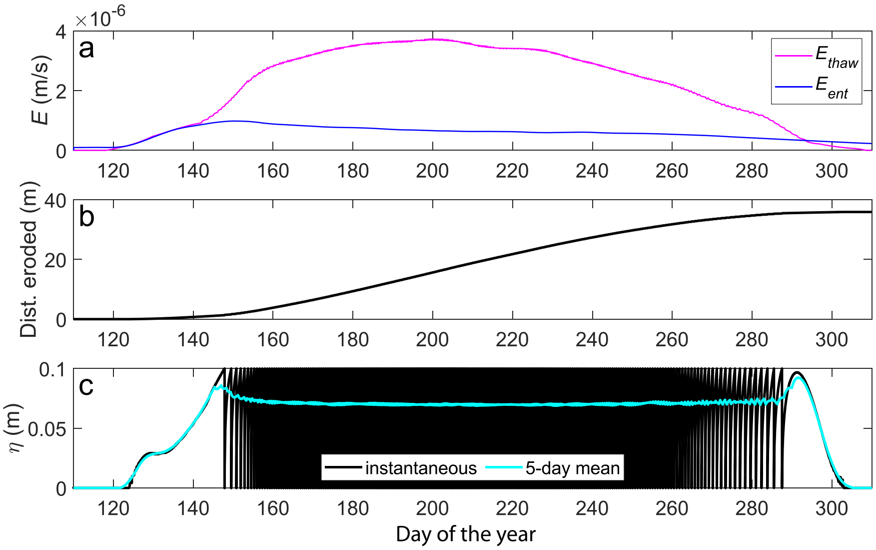

Figure 9. Bank erosion rate for Yukon River as a function of discharge (Figure 7a) and water temperature (Figure 7b) from the modern hydrograph with a 10 cm threshold for thaw layer failure. (a) Modeled bank thaw (E_{thaw}) and sediment entrainment (E_{ent}) rates. (b) Cumulative bank erosion versus day of the year. (c) Modeled instantaneous (black line) and 5-day moving mean (light blue) thaw layer thickness (η) versus day of the year, with abrupt drops in η signifying thawed layer failures that occurred when $\eta > 10$ cm.

However, $E_{\mathrm{thaw}} \sim UT_w$ and $E_{\mathrm{ent}} \sim U^2$, and U varied from approximately 0–3 m/s, while T_w varied from approximately 0–20°C. Therefore, late-summer floods saw some increase in entrainment rates as U increased, but warm summer water temperatures caused E_{thaw} to remain much higher than E_{ent} throughout the flood and prevented thaw-limited conditions from developing. Importantly, this model run did not consider the effect of bank collapse upon thaw, which has been observed to modulate erosion rates (Chassiot et al., 2020; Shur et al., 2021), and was considered in the next section.

5.4. Buffered Regime With Intermittent Bank Failure

To understand how periodic failures of the thawed layer, which are commonly observed in permafrost environments (Kanevskiy et al., 2016; Walker et al., 1987), might affect bank erosion rates, we added a criterion to the model where thawed sediment will be removed whenever a critical thickness (η_{fail}; m) is exceeded (Figure 9). This simplified model for bank failure accounted for subaqueous mass failure in addition to ongoing sediment entrainment (Equation 2). We ran the model using the modern annual discharge and water temperature curves for the Yukon River at Stevens Village (Figures 7a and 7b) but imposed a critical thickness of 10 cm for thawed layer failure. We assumed that failure occurred at the thaw front because of the significant difference in tensile strength between the thawed and frozen bank materials. This produced hundreds of bank failures and a total of 36.17 m of bank erosion during the summer months (Figures 9b and 9c). While models without failure showed that the rate of bank thaw (E_{thaw}) reached a similar rate as erosion due to sediment entrainment (E_{ent}), the buffered regime produced consistently high E_{thaw} throughout the summer months (Figure 9b). This was because bank thaw rates decreased as the thawed layer developed and insulated the bank, producing a curved concave-down profile of thawed layer thickness between failure events (Figure 9c). The decrease in the thawed layer growth rate as the layer thickened produced a ~7 cm 5-day moving average thickness, while constant thaw rates produced a thawed layer up to ~30 cm thick. The erosion rates produced with the periodic failure model were four times greater than models that did not include thaw layer failure, indicating that the stability of the thawed layer might be a primary control on permafrost riverbank erosion rates. For instance, with a higher threshold, we might expect fewer failures and slower erosion rates, while a lower threshold could produce more failures and faster total erosion rates.

To explore the parameter space of the bank failure model, we ran the 1 mm sand and 1 cm gravel models for our base case hydraulics. We maintained a constant 10°C water temperature over 1 day and modeled a range of critical thicknesses (η_{fail}) to understand model behavior given subaqueous bank failures. Hydraulic conditions in our base case were insufficient to entrain 1 cm gravel, so no erosion occurred except due to bank failure, but flow was

21699011, 2024, 4, Downloaded from https://agupubs.onlinelibrary.wiley.com/doi/10.1029/2023JF007452 by California Inst of Technology, Wiley Online Library on [14/06/2024]. See the Terms and Conditions (https://onlinelibrary.wiley.com/terms-and-conditions) on Wiley Online Library for rules of use; OA articles are governed by the applicable Creative Commons License

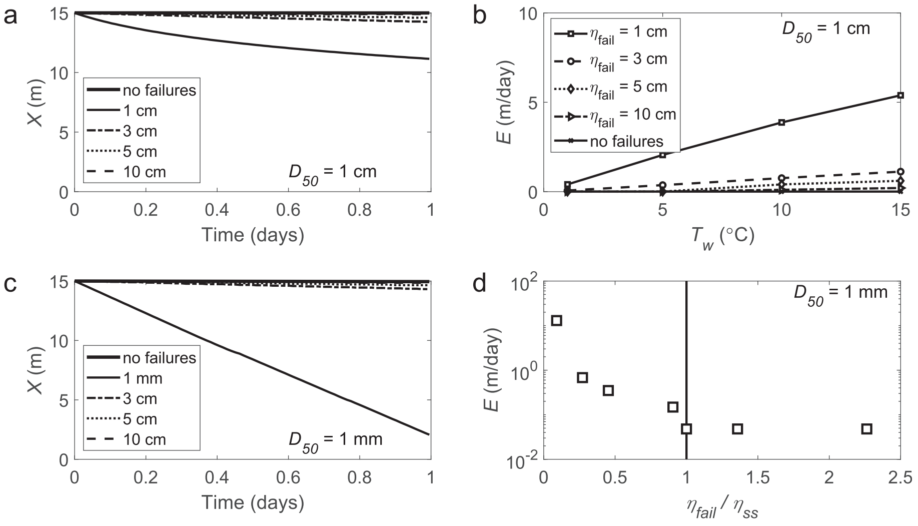

Figure 10. Model results for the buffered regime, which has periodic thawed-layer failure. (a) Bank front location for immobile 1 cm diameter gravel with 10°C river water models with imposed threshold for failure when the thickness of the thawed layer exceeds 1, 3, 5, and 10 cm, and a case without failure. (b) Erosion rates for 1 cm gravel with varying η_{fail} versus water temperature. (c) Bank front location for mobile 1 mm coarse sand with 10°C river water models with an imposed threshold for failure when the thickness of the thawed layer exceeds 0.1, 3, 5, and 10 cm, plus a case without failure. (d) Erosion rates for 1 mm sand with varying ratios of η_{fail}/η_{ss}.

sufficient to erode 1 mm sand. We compared model results to a case with no failures for 1 mm sand, where the thaw layer developed to a steady-state thickness. For the 1 cm gravel, we compared erosion rates for different water temperatures and failure thresholds.

For the 1 cm gravel case, we found that banks with a low threshold of failure for thawed sediment tended to erode very rapidly, while banks with a high failure threshold did not experience any failures and did not erode (Figure 10a). For the 1 mm sand case, very slow bank erosion occurred in the absence of failure, but bank erosion with failure produced rates orders of magnitude higher at over 10 m/day (Figure 10c). In all cases, the bank surface temperature increased as the thawed layer thickened, decreasing the total heat flux to the bank and the temperature gradient within the thawed layer. These effects caused a decrease in the thaw rate for permafrost in banks with larger η. However, small values of η_{fail} maintained conditions where permafrost thaw was rapid and the bank rapidly eroded. When η_{fail} was greater than η_{ss}, we saw constant entrainment-limited erosion rates, while a decreasing ratio of $\eta_{\mathrm{fail}}/\eta_{ss}$ caused a nonlinear increase in erosion rates due to the persistence of a high thermal gradient within the thawed portion of the bank (Figure 10d).

Next, we varied the water temperature and η_{fail} for the 1 cm gravel case (Figure 10b). Higher water temperatures produced faster bank erosion rates for the same relative bank stability ($\eta_{\mathrm{fail}}/\eta_{ss}$) due to a higher thermal gradient within the thawed region of the bank. The rate of bank erosion was a linear function of water temperature, but banks with smaller values for η_{fail} had a much stronger dependence on water temperature than banks with higher values of η_{fail}. For example, increasing η_{fail} from 1 to 3 cm decreased bank erosion rates by a factor of ~5. This occurred because bank failure frequency was a function of water temperature since higher water temperatures produced a greater initial thaw rate and grew η more rapidly. This supported that bank erosion rates were highly sensitive to the value of η_{fail} since increasing η_{fail} by an order of magnitude increased erosion rates by over two orders of magnitude (Figure 10d), while increasing water temperature by an order of magnitude increased erosion rates by less than a factor of 10 (Figure 10b). Therefore, bank erosion in the buffered regime was linearly dependent on water temperature despite the presence of a thawed layer for almost the entirety of the model run.

6. Discussion

6.1. Analytical Approximation for Thawed-Layer Thickness

Results indicated that the numerical model of permafrost riverbank thaw and periodic collapse can produce thicknesses of thawed layers similar to those observed in the field (Figure 1). Thawed layer thickness rapidly

21699011, 2024, 4, Downloaded from https://agupubs.onlinelibrary.wiley.com/doi/10.1029/2023JF007452 by California Inst of Technology, Wiley Online Library on [14/06/2024]. See the Terms and Conditions (https://onlinelibrary.wiley.com/terms-and-conditions) on Wiley Online Library for rules of use; OA articles are governed by the applicable Creative Commons License

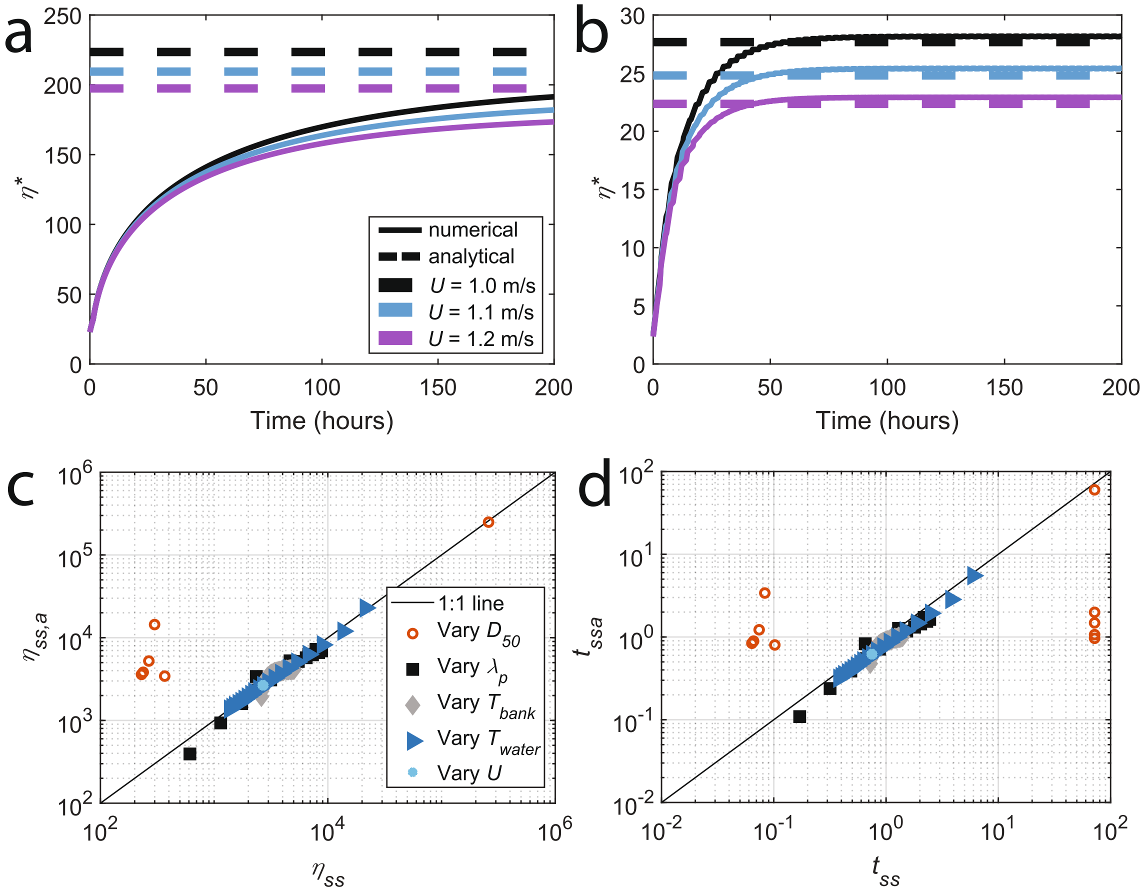

Figure 11. Development of an analytical approximation for steady-state thaw layer thickness. (a) Numerical model runs do not match the analytical approximation for our base case and conditions representative of natural rivers because a nonlinear temperature profile develops in the thawed layer. (b) Validation of numerical model versus analytical approximations using conditions not representative of natural rivers. Model is run under constant hydraulic conditions for the base case, with thermal conductivities and diffusivity multiplied by a factor of 100 and $\lambda_p = 0.5$ to produce a linear temperature profile through the thawed layer. (c) Comparison of steady-state thaw layer thickness from numerical (x-axis) solutions from Figures 7 and 8 and analytical model approximations (y-axis) using Equations 33 and 41. (d) Comparison of the timescale to reach steady-state in the numerical solutions shown in Figures 7 and 8 with an analytical model (Equation 42).

adjusted to river hydraulic and thermal conditions in timescales typical of hours (Figure 6), which was shorter than the forcing timescales for most rivers. Therefore, we expect that most natural riverbanks should be near the steady state, and it is useful to have an analytical approximation for steady-state thawed layer thickness. We derived such an approximation in Section 3.4 (Equation 34), but this approximation assumed there was a linear temperature profile through the thawed layer, and our analysis revealed that this is rarely the case in natural river systems. In Figure 11a, we compare the numerical and analytical approximations for our base case with slight differences in river flow velocity and the results significantly disagree. Therefore, in this section, we develop an empirical fit between our model runs to steady state and the analytical approximation.

We validated the numerical model against the steady-state model for cases where a linear temperature profile was expected to form through the thawed layer (Figure 11b). To do so, we ran the model base case with the thermal conductivities and diffusivities of the frozen and thawed bank multiplied by 100. We also set $\lambda_p = 0.5$, $T_w = 0.1$°C, and $T_0 = 0$°C and evaluated the model for U ranging from 1 to 1.2 m/s. The numerical model results converged to the analytical approximation (Equation 34) after 100 hr. These bank thermal properties were two orders of magnitude greater than those of frozen or liquid water or sand, so they represented a theoretical case evaluated for the purpose of model validation. Thus, while the numerical model agreed with the analytical model, confirming that it was implemented correctly, the analytical model did not produce realistic thaw layer thicknesses for conditions present in natural rivers.

21699011, 2024, 4, Downloaded from https://agupubs.onlinelibrary.wiley.com/doi/10.1029/2023JF007452 by California Inst of Technology, Wiley Online Library on [14/06/2024]. See the Terms and Conditions (https://onlinelibrary.wiley.com/terms-and-conditions) on Wiley Online Library for rules of use; OA articles are governed by the applicable Creative Commons License

Realistic values for river hydraulics and permafrost characteristics rarely satisfy the linear temperature profile assumption required to solve the analytical approximation. Therefore, we developed a semi-empirical approximation by fitting a nondimensional scaling factor s that can be multiplied to the right-hand side of Equation 34 to reproduce results with realistic nonlinear temperature profiles. We calculate s as the ratio of the unsteady and analytical approximations and find:

$$s = 10481\left(E^*_{\text{ent}}\right)^{0.118}\left(\left|T^*_0\right|\right)^{0.128}\left(U^*\right)^{2.090}\left(C^*_h\right)^{1.711}\left(C^*_{ic}\right)^{-5.722}\left(T^*_w\right)^{-1.945}\left(K^*_{ts}\right)^{-0.559}. \tag{41}$$

We fit s using a linear regression model (Matlab function fitlm.m) to the $\log_{10}$ of the absolute values of the nondimensional variables on the right-hand side of Equation 34 using the model results from Figures 7 and 8. All terms had $p < 0.05$ except for E_{ent}*, which we included ($p = 0.40$). This produced Equation 41, which has $R^2 = 0.849$ in log-log space (Figure 11c). Solving Equation 34 using a value of s calculated from Equation 41 produced an analytical approximation of steady-state thawed layer thickness accurate to cm-scale for the range of terrestrial permafrost environments. This fit should only be used for values within those we explored in Figures 7 and 8 and provides a good fit for rivers similar to the Yukon River near Stevens Village, AK, which serves as the base case. Thus, Equation 41 provides an analytical method to estimate thaw layer thickness at steady-state conditions without running the full numerical model.

We used a similar fitting method to develop an approximation for the timescale required to reach the steady state ($t_{ss,a}$). We fit a linear model of $\log_{10}(t_{ss,a})$ to the $\log_{10}$ of the absolute values of the nondimensional variables in Equation 34 using model results from Figures 7 and 8 and Matlab function fitlm.m. All nondimensional variables had significance of $p < 0.05$, so we included all variables to produce a fit with $R^2 = 0.330$ in log-log space (Figure 11d). The analytical approximation is

$$t_{ss,a} = 0.592\left(E^*_{\text{ent}}\right)^{-0.888}\left(\left|T^*_0\right|\right)^{0.128}\left(U^*\right)^{2.103}\left(C^*_h\right)^{1.781}\left(C^*_{ic}\right)^{-4.136}\left(T^*_w\right)^{-0.953}\left(K^*_{ts}\right)^{-0.226}, \tag{42}$$

which provides an accurate estimation of the timescale to reach a steady state for rivers similar to the Yukon at Stevens Village.

6.2. Broader Implications of Model

Our results indicate that the development of a thawed layer is important to modulate permafrost riverbank erosion rates. Purely thaw-limited erosion models predict very rapid erosion that exceeds the ability of many rivers to entrain and transport sediment off their banks (Figures 7 and 8). Therefore, thaw-limited conditions should only persist for a very short period at the start of the melt season for most natural rivers. When bank thaw rates exceed entrainment rates, our model reproduces field observations of a thawed layer that insulates the underlying frozen bank material and slows pore ice melting (Gautier & Costard, 2000; Scott, 1978). For cases with non-zero entrainment, the pore ice melt rate gradually slows to equal the sediment entrainment rate and the thawed layer approaches a steady-state thickness, which typically occurs over timescales of hours to days (Figures 5 and 6). Because this timescale is shorter than the timescales for changing river water discharge and temperature, most natural rivers can be considered at a steady state even under transient conditions and Equation 41 can be used to approximate the thawed layer thickness.

Bank grain size has a significant effect on thawed layer thickness, with coarser grains generally having thicker thawed layers (Figure 4). Coarser gravel banks have greater pore water flow, so heat is advected more rapidly into the bank and can more efficiently thaw pore ice (Wankiewicz, 1984). Coarser grains also significantly disrupt the viscous flow sublayer over the bank, which can reduce heat transfer to the bank and cause a decline in nondimensional thawed layer thickness as a function of grain size (Douglas, Miller, et al., 2023). However, very coarse-grained banks can be above the threshold for sediment entrainment under most flow conditions (Parker, 1978), which causes entrainment rates to be zero and produces a very thick thawed layer. While the result of zero entrainment at low flows for coarse sediment might be in part due to our choice of sediment entrainment function (Equation 2) and critical Shields stress (Equation 37; Wilcock et al., 1996), we expect that bank erosion rates will nevertheless remain very low and allow a thick thawed layer to develop substituting other reasonable gravel entrainment relations. In contrast, fine-grained banks often have thin thawed layers because both sediment entrainment and heat transfer to the bank are slower than in sand. Fine-grained banks may also experience

21699011, 2024, 4, Downloaded from https://agupubs.onlinelibrary.wiley.com/doi/10.1029/2023JF007452 by California Inst of Technology, Wiley Online Library on [14/06/2024]. See the Terms and Conditions (https://onlinelibrary.wiley.com/terms-and-conditions) on Wiley Online Library for rules of use; OA articles are governed by the applicable Creative Commons License

transitional or laminar, instead of hydraulically rough, near-bank fluid flow ($Re_{ks} < 100$), which is expected to decrease the coefficient of heat transfer (Equation 8) and thus the rate of bank thaw (Yaglom & Kader, 1974). Sediment is difficult to entrain in the transitional and laminar regimes as the critical Shields number increases for particle Reynolds numbers corresponding to silt (Vanoni, 2006). Therefore, tradeoffs between thaw and entrainment rates cause coarse-grained banks to develop thicker thawed layers than fine-grained banks, in agreement with field observations (Scott, 1978).

While steady-state conditions develop within days for most cases, model results indicate that transient states can be important for certain cases. For example, when bank entrainment rates are zero due to slow water flow velocities or coarse grain sizes, the thawed layer can grow indefinitely (Figure 4). If the thawed layer thickness exceeds the strength of the material, it can fail and produce rapid erosion rates (Figure 10). However, model results indicate that if the thawed layer does not fail, its presence will not cause a subsequent increase in erosion rates during late-season floods (Figure 8). This is because erosion rates are entrainment-limited for realistic late-season conditions and rapidly approach a steady-state thawed layer thickness in the absence of periodic failures.

Our model predicts two regimes when sediment entrainment rates are lower than permafrost thaw rates: the entrainment-limited and buffered regimes. In the entrainment-limited regime, bank erosion is governed by the sediment entrainment rate and follows the same governing equations as riverbank erosion in non-permafrost regions (Douglas, Miller, et al., 2023; Douglas, Dunne, & Lamb, 2023). Our results also describe a new regime, which we term the buffered regime, where the thawed layer becomes unstable and fails when it grows past a given thickness (Figure 10). Importantly, bank erosion rates in the buffered regime are sensitive to water temperature because warmer water temperatures cause the thawed layer to thicken and fail more rapidly, while entrainment-limited banks are insensitive to water temperature. Therefore, our mathematical description of the buffered regime can reconcile theoretical predictions that permafrost bank thaw rates should exceed sediment entrainment rates for much of the summer with field observations of riverbanks with exposed or thinly covered permafrost in late summer (Fuchs et al., 2020; Kanevskiy et al., 2016) and remote sensing observations of slow migration for permafrost rivers (Rowland et al., 2019; Rowland, Crosby, et al., 2023; Rowland, Schwenk, et al., 2023).

We expect that our model results will apply to sand- and gravel-bedded permafrost riverbanks, though model applicability is limited by its 1D framework. We model bank sediment critical shear stress (Parker et al., 2003) and roughness (Colebrook, 1939; Rickenmann & Recking, 2011) using relations that are valid for hydraulically smooth and rough flow appropriate to silt through gravel, though different roughness relations should be used for banks containing cobbles or cohesive sediment (Ferguson, 2007; Ternat et al., 2008). We also do not consider the effects of vegetation on increasing riverbank cohesion or altering hydrologic properties, which are known to affect temperate river systems (e.g., Bankhead et al., 2017; Vargas-Luna et al., 2019) and are expected to affect permafrost river systems (Ielpi et al., 2023; Scott, 1978). In addition, our 1D model assumes homogeneous permafrost and uses a simple threshold thaw distance for failure. Developing a 2D or 3D model requires considering the heterogeneities in bank ice distribution and their potential as failure planes (Barnhart et al., 2014; Kanevskiy et al., 2016), allowing for variable locations bank failure (Zhang et al., 2021; Zhao et al., 2021, 2022), and tracking the erosion of sediment following mass failure (e.g., Asahi et al., 2013; Parker et al., 2011). This includes constraining forces resulting from hydrologic connectivity between the river and its banks (Kurylyk et al., 2016; Zhao et al., 2020) as well as a more detailed investigation of interactions between riverbank pore water flow and heat transfer (Rowland, Crosby, et al., 2023; Rowland, Schwenk, et al., 2023). Extending our model to riverbanks that are exposed subaerially or experience periodic inundation will also require considering heat fluxes due to insolation and air temperature (Walker et al., 1987; Walvoord & Kurylyk, 2016). Ultimately, our model validation is significantly limited by the availability of detailed characterizations of thaw layer thickness, riverbank sedimentology, and erosional processes on natural permafrost riverbanks (Rowland & Coon, 2016). Obtaining these measurements from a wide variety of permafrost river systems is crucial for developing a 3D model of permafrost riverbank erosion.

Determining whether permafrost riverbanks are in the buffered or entrainment-limited regimes during summer months is important for predicting how these rivers will respond to climate change. River discharge (Peterson et al., 2002) and water temperature (Liu et al., 2005; Yang & Peterson, 2017) are increasing in response to climatic warming. Water temperature affects the rate of heat transfer between the river and the bank, and effects on the sediment entrainment rate can be accounted for using existing theory (Syvitski et al., 2019). River discharge

21699011, 2024, 4, Downloaded from https://agupubs.onlinelibrary.wiley.com/doi/10.1029/2023JF007452 by California Inst of Technology, Wiley Online Library on [14/06/2024]. See the Terms and Conditions (https://onlinelibrary.wiley.com/terms-and-conditions) on Wiley Online Library for rules of use; OA articles are governed by the applicable Creative Commons License

increases flow depth and velocity and is predicted to cause an increase in both thaw-limited and entrainment-limited bank erosion rates via Equations 2 and 8. However, the buffered regime exhibits a complicated dependence on river discharge and temperature, with rates increasing nonlinearly with water temperature, whereas the entrainment-limited regime does not depend on water temperature. These two regimes are difficult to distinguish in the field since both should have a thawed layer present on the bank surface, though it is important to do so because this determines whether bank erosion rates should increase in response to warming river waters. Determining which permafrost rivers fall into the buffered versus entrainment-limited regimes is crucial for predicting how riverbank erosion rates will respond to ongoing climate change.

7. Conclusions

Field observations and numerical models disagree on the governing processes and rates of permafrost riverbank erosion. To address this knowledge gap, we developed a 1D model that includes bank sediment erosion, heat transfer from the river to the bank, and phase changes within the frozen bank. The model produces three regimes: thaw-limited, entrainment-limited, and buffered erosion. Thaw-limited erosion only occurs during winter months and immediately following ice break-up, when water temperatures are very low and riverine sediment transport capacity is very high. When banks become entrainment-limited for much of the summer, the model produces a thin thawed layer that can either reach a constant thickness to match bank erosion rates or grow indefinitely when river flow is insufficient to erode thawed bank sediment. We parameterized a highly simplified model of periodic thawed layer failure to investigate the buffered regime and found that erosion rates are rapid and remain sensitive to water temperature. In general, the model is very sensitive to bank material properties, such as grain size and pore ice content, but relatively insensitive to bank temperature. Higher water temperatures increase the rates of thaw-limited and buffered erosion, while higher discharges increase all erosion mechanisms. A comparison of annual hydrologic data at Stevens Village on the Yukon River suggests that our model produces plausible bank erosion rates over the course of annual water temperature and discharge cycles. This model indicates that thaw-limited conditions occur very rarely, so many Arctic rivers likely experience entrainment-limited or buffered erosion for at least part of the year. Distinguishing between these processes is important for predicting the rates of bank erosion in response to changing climate, since that will determine whether erosion is sensitive to river water temperature (in the buffered regime) or only discharge.

Data Availability Statement

Data for permafrost probe measurements are available in the Supporting Information and at Douglas, Blankenship, et al. (2023). Soil bulk density and water content data are available from Douglas et al. (2022). Data for ground temperature at Huslia (site ID US O-82) from the Global Terrestrial Network for Permafrost (GTN-P) Database from Biskaborn et al. (2015). Model scripts are available at M. M. Douglas (2023).

Acknowledgments
The authors would like to thank the Koyukon Athabascans, Chief Carl Burgett, and the Huslia Tribal Council for access to their land, and USFWS Koyukuk National Wildlife Refuge for research permitting and logistical assistance. We acknowledge Shawn Huffman, Alvin Attla, Darin Dayton, Charlene Mayo, Mary Ann Sam, and Virgil Umphenour for field logistical support and local expertise. We would also like to thank Rain Blankenship, Austin Chadwick, Hannah Dion-Kirshner, Kieran Dunne, Emily Geyman, Yutian Ke, Preston C. Kemeny, Gen K. Li, John Magyar, Edda Mutter, Justin Nghiem, Anastasia Piliouras, Jocelyn Reahl, Joel Rowland, Jon Schwenk, Emily Seelen, Isabel Smith, Josh West, and Lisa Winter for assistance in collecting field data; Kim Litwin Miller, Bill Dietrich, Chris Paola, and the Caltech 2018 Ge126 course for fruitful discussions; and editor Marisa Repasch as well as Kun Zhao and three anonymous reviewers for their helpful feedback. In addition, the authors acknowledge funding from the Resnick Sustainability Institute at Caltech, NSF Awards 2127442 and 2031532, and the National Defense Science and Engineering Graduate Fellowship.

References

Akagawa, S., & Nishisato, K. (2009). Tensile strength of frozen soil in the temperature range of the frozen fringe. *Cold Regions Science and Technology*, *57*(1), 13–22. https://doi.org/10.1016/j.coldregions.2009.01.002

Anisimov, O. A., Shiklomanov, N. I., & Nelson, F. E. (1997). Global warming and active-layer thickness: Results from transient general circulation models. *Global and Planetary Change*, *15*(3), 61–77. https://doi.org/10.1016/S0921-8181(97)00009-X

Asahi, K., Shimizu, Y., Nelson, J., & Parker, G. (2013). Numerical simulation of river meandering with self-evolving banks. *Journal of Geophysical Research: Earth Surface*, *118*(4), 2208–2229. https://doi.org/10.1002/jgrf.20150

Bankhead, N. L., Thomas, R. E., & Simon, A. (2017). A combined field, laboratory and numerical study of the forces applied to, and the potential for removal of, bar top vegetation in a braided river. *Earth Surface Processes and Landforms*, *42*(3), 439–459. https://doi.org/10.1002/esp.3997

Barnhart, K. R., Anderson, R. S., Overeem, I., Wobus, C., Clow, G. D., & Urban, F. E. (2014). Modeling erosion of ice-rich permafrost bluffs along the Alaskan Beaufort Sea coast. *Journal of Geophysical Research: Earth Surface*, *119*(5), 1155–1179. https://doi.org/10.1002/2013JF002845

Barree, R. D., & Conway, M. W. (2004). Beyond beta factors: A complete model for Darcy, Forchheimer, and trans-Forchheimer flow in porous media. In *Presented at the SPE Annual Technical Conference and Exhibition, OnePetro*. https://doi.org/10.2118/89325-MS

Bear, J. (1972). In *Dynamics of fluids in porous media* (Vol. 61). American Elsevier Publishing Company.

Beckermann, C., & Viskanta, R. (1988). Natural convection solid/liquid phase change in porous media. *International Journal of Heat and Mass Transfer*, *31*(1), 35–46. https://doi.org/10.1016/0017-9310(88)90220-7

Biskaborn, B. K., Lanckman, J.-P., Lantuit, H., Elger, K., Streletskiy, D. A., Cable, W. L., & Romanovsky, V. E. (2015). The new database of the global terrestrial network for permafrost (GTN-P). *Earth System Science Data*, *7*(2), 245–259. https://doi.org/10.5194/essd-7-245-2015

Brabets, T. P., & Walvoord, M. A. (2009). Trends in streamflow in the Yukon River basin from 1944 to 2005 and the influence of the Pacific Decadal Oscillation. *Journal of Hydrology*, *371*(1), 108–119. https://doi.org/10.1016/j.jhydrol.2009.03.018

Bronen, R. (2013). *Climate-induced displacement of Alaska native communities (Project on internal displacement)* (p. 25). Brookings Institute.

21699011, 2024, 4, Downloaded from https://agupubs.onlinelibrary.wiley.com/doi/10.1029/2023JF007452 by California Inst of Technology, Wiley Online Library on [14/06/2024]. See the Terms and Conditions (https://onlinelibrary.wiley.com/terms-and-conditions) on Wiley Online Library for rules of use; OA articles are governed by the applicable Creative Commons License

21699011, 2024, 4, Downloaded from https://agupubs.onlinelibrary.wiley.com/doi/10.1029/2023JF007452 by California Inst of Technology, Wiley Online Library on [14/06/2024]. See the Terms and Conditions (https://onlinelibrary.wiley.com/terms-and-conditions) on Wiley Online Library for rules of use; OA articles are governed by the applicable Creative Commons License

Charney, J. G., FjÖrtoft, R., & Neumann, J. V. (1950). Numerical integration of the barotropic vorticity equation. *Tellus*, *2*(4), 237–254. https://doi.org/10.3402/tellusa.v2i4.8607

Chassiot, L., Lajeunesse, P., & Bernier, J.-F. (2020). Riverbank erosion in cold environments: Review and outlook. *Earth-Science Reviews*, *207*, 103231. https://doi.org/10.1016/j.earscirev.2020.103231

Clement, D. T. (1999). *Fluvial geomorphology of the Yukon River, Yukon Flats, Alaska (Master of Science)*. University of Calgary.

Colebrook, C. F. (1939). Turbulent flow in pipes, with particular reference to the transition region between the smooth and rough pipe laws. *Journal of the Institution of Civil Engineers*, *11*(4), 133–156. https://doi.org/10.1680/ijoti.1939.13150

Costard, F., Dupeyrat, L., Gautier, E., & Carey-Gailhardis, E. (2003). Fluvial thermal erosion investigations along a rapidly eroding river bank: Application to the Lena River (central Siberia). *Earth Surface Processes and Landforms*, *28*(12), 1349–1359. https://doi.org/10.1002/esp.592

Costard, F., Gautier, E., Fedorov, A., Konstantinov, P., & Dupeyrat, L. (2014). An assessment of the erosion potential of the fluvial thermal process during ice breakups of the Lena River (Siberia). *Permafrost and Periglacial Processes*, *25*(3), 162–171. https://doi.org/10.1002/ppp.1812

Courant, R., Friedrichs, K., & Lewy, H. (1928). Über die partiellen Differenzengleichungen der mathematischen Physik. *Mathematische Annalen*, *100*(1), 32–74. https://doi.org/10.1007/BF01448839

Cozzetto, K., Chief, K., Dittmer, K., Brubaker, M., Gough, R., Souza, K., et al. (2014). Climate change impacts on the water resources of American Indians and Alaska Natives in the U.S. In J. K. Maldonado, B. Colombi, & R. Pandya (Eds.), *Climate change and indigenous peoples in the United States: Impacts, experiences and actions* (pp. 61–76). Springer International Publishing. https://doi.org/10.1007/978-3-319-05266-3_6

Debol'skaya, E. I., & Ivanov, A. V. (2020). Comparative analysis of models of thermoerosion-induced channel deformations in rivers of permafrost zone. *Water Resources*, *47*(1), 77–86. https://doi.org/10.1134/S0097807820010054

Douglas, M., Blankenship, R., Chadwick, A., Dunne, K., Fischer, W., Geyman, E., et al. (2023). Geomorphic mapping and permafrost occurrence on the Koyukuk River floodplain near Huslia, Alaska [Dataset]. *ESS-DIVE*. https://doi.org/10.15485/2204419

Douglas, M. M. (2023). madisonmdouglas/permafrost-riverbank: Permafrost bank erosion model May 22, 2023 Release (Version 1) [Software]. *Zenodo*. https://doi.org/10.5281/zenodo.7958708

Douglas, M. M., Dunne, K. B. J., & Lamb, M. P. (2023). Sediment entrainment and slump blocks limit permafrost riverbank erosion. *Geophysical Research Letters*, *50*(11), e2023GL102974. https://doi.org/10.1029/2023GL102974

Douglas, M. M., Li, G. K., Fischer, W. W., Rowland, J. C., Kemeny, P. C., West, A. J., et al. (2022). Organic carbon burial by river meandering partially offsets bank erosion carbon fluxes in a discontinuous permafrost floodplain. *Earth Surface Dynamics*, *10*(3), 421–435. https://doi.org/10.5194/esurf-10-421-2022

Douglas, M. M., Miller, K. L., Schmeer, M. N., & Lamb, M. P. (2023). Ablation-limited erosion rates of permafrost riverbanks. *Journal of Geophysical Research: Earth Surface*, *128*(8), e2023JF007098. https://doi.org/10.1029/2023JF007098

Dupeyrat, L., Costard, F., Randriamazaoro, R., Gailhardis, E., Gautier, E., & Fedorov, A. (2011). Effects of ice content on the thermal erosion of permafrost: Implications for coastal and fluvial erosion. *Permafrost and Periglacial Processes*, *22*(2), 179–187. https://doi.org/10.1002/ppp.722

Ferguson, R. (2007). Flow resistance equations for gravel- and boulder-bed streams. *Water Resources Research*, *43*(5). https://doi.org/10.1029/2006WR005422

Fuchs, M., Nitze, I., Strauss, J., Günther, F., Wetterich, S., Kizyakov, A., et al. (2020). Rapid fluvio-thermal erosion of a yedoma permafrost cliff in the Lena River delta. *Frontiers in Earth Science*, *8*. https://doi.org/10.3389/feart.2020.00336

Gautier, E., & Costard, F. (2000). Les systèmes fluviaux à chenaux anastomosés en milieu périglaciaire: La Léna et ses principaux affluents (Sibérie centrale). *Géographie Physique et Quaternaire*, *54*(3), 327–342. https://doi.org/10.7202/005647ar

Gautier, E., Dépret, T., Cavero, J., Costard, F., Virmoux, C., Fedorov, A., et al. (2021). Fifty-year dynamics of the Lena River islands (Russia): Spatio-temporal pattern of large periglacial anabranching river and influence of climate change. *The Science of the Total Environment*, *783*, 147020. https://doi.org/10.1016/j.scitotenv.2021.147020

Ghisalberti, M. (2009). Obstructed shear flows: Similarities across systems and scales. *Journal of Fluid Mechanics*, *641*, 51–61. https://doi.org/10.1017/S0022112009992175

Hjort, J., Karjalainen, O., Aalto, J., Westermann, S., Romanovsky, V. E., Nelson, F. E., et al. (2018). Degrading permafrost puts Arctic infrastructure at risk by mid-century. *Nature Communications*, *9*(1), 5147. https://doi.org/10.1038/s41467-018-07557-4

Holmes, R. M., McClelland, J. W., Peterson, B. J., Tank, S. E., Bulygina, E., Eglinton, T. I., et al. (2012). Seasonal and annual fluxes of nutrients and organic matter from large rivers to the Arctic Ocean and surrounding seas. *Estuaries and Coasts*, *35*(2), 369–382. https://doi.org/10.1007/s12237-011-9386-6

Hsu, C. T., & Cheng, P. (1990). Thermal dispersion in a porous medium. *International Journal of Heat and Mass Transfer*, *33*(8), 1587–1597. https://doi.org/10.1016/0017-9310(90)90015-m

Ielpi, A., Lapôtre, M. G. A., Finotello, A., & Roy-Léveillée, P. (2023). Large sinuous rivers are slowing down in a warming Arctic. *Nature Climate Change*, *13*(4), 1–7. https://doi.org/10.1038/s41558-023-01620-9

Kader, B. A., & Yaglom, A. M. (1972). Heat and mass transfer laws for fully turbulent wall flows. *International Journal of Heat and Mass Transfer*, *15*(12), 2329–2351. https://doi.org/10.1016/0017-9310(72)90131-7

Kanevskiy, M., Shur, Y., Strauss, J., Jorgenson, T., Fortier, D., Stephani, E., & Vasiliev, A. (2016). Patterns and rates of riverbank erosion involving ice-rich permafrost (yedoma) in northern Alaska. *Geomorphology*, *253*, 370–384. https://doi.org/10.1016/j.geomorph.2015.10.023

Karjalainen, O., Aalto, J., Luoto, M., Westermann, S., Romanovsky, V. E., Nelson, F. E., et al. (2019). Circumpolar permafrost maps and geohazard indices for near-future infrastructure risk assessments. *Scientific Data*, *6*(1), 1–16. https://doi.org/10.1038/sdata.2019.37

Kobayashi, N., & Aktan, D. (1986). Thermoerosion of frozen sediment under wave action. *Journal of Waterway, Port, Coastal, and Ocean Engineering*, *112*(1), 140–158. https://doi.org/10.1061/(ASCE)0733-950X(1986)112:1(140)

Kudryavtsev, V. A., Garagulya, L. S., & Melamed, V. G. (1977). *Fundamentals of frost forecasting in geological engineering investigations (Osnovy Merzlotnogo Prognoza pri Inzhenerno-Geologicheskikh Issledovaniyakh)*. Hanover, NH: Cold Regions Research and Engineering Lab.

Kurylyk, B. L., Hayashi, M., Quinton, W. L., McKenzie, J. M., & Voss, C. I. (2016). Influence of vertical and lateral heat transfer on permafrost thaw, peatland landscape transition, and groundwater flow. *Water Resources Research*, *52*(2), 1286–1305. https://doi.org/10.1002/2015WR018057

Kuwata, Y. (2021). Direct numerical simulation of turbulent heat transfer on the Reynolds analogy over irregular rough surfaces. *International Journal of Heat and Fluid Flow*, *92*, 108859. https://doi.org/10.1016/j.ijheatfluidflow.2021.108859

Lafrenière, M. J., & Lamoureux, S. F. (2019). Effects of changing permafrost conditions on hydrological processes and fluvial fluxes. *Earth-Science Reviews*, *191*, 212–223. https://doi.org/10.1016/j.earscirev.2019.02.018

Lamb, M. P., Brun, F., & Fuller, B. M. (2017). Hydrodynamics of steep streams with planar coarse-grained beds: Turbulence, flow resistance, and implications for sediment transport. *Water Resources Research*, *53*(3), 2240–2263. https://doi.org/10.1002/2016WR019579

Lange, M. A., & Ahrens, T. J. (1983). The dynamic tensile strength of ice and ice-silicate mixtures. *Journal of Geophysical Research*, *88*(B2), 1197–1208. https://doi.org/10.1029/JB088iB02p01197

Lapotre, M. G., & Lamb, M. P. (2018). Substrate controls on valley formation by groundwater on Earth and Mars. *Geology*, *46*(6), 531–534. https://doi.org/10.1130/G40007.1

Lininger, K. B., & Wohl, E. (2019). Floodplain dynamics in North American permafrost regions under a warming climate and implications for organic carbon stocks: A review and synthesis. *Earth-Science Reviews*, *193*, 24–44. https://doi.org/10.1016/j.earscirev.2019.02.024

Lininger, K. B., Wohl, E., & Rose, J. R. (2018). Geomorphic controls on floodplain soil organic carbon in the Yukon Flats, Interior Alaska, from reach to river basin scales. *Water Resources Research*, *0*(0), 1934–1951. https://doi.org/10.1002/2017WR022042

Lininger, K. B., Wohl, E., Rose, J. R., & Leisz, S. J. (2019). Significant floodplain soil organic carbon storage along a large high-latitude river and its tributaries. *Geophysical Research Letters*, *46*(4), 2121–2129. https://doi.org/10.1029/2018GL080996

Litwin, K. L., Zygielbaum, B. R., Polito, P. J., Sklar, L. S., & Collins, G. C. (2012). Influence of temperature, composition, and grain size on the tensile failure of water ice: Implications for erosion on Titan. *Journal of Geophysical Research*, *117*(E8), E08013. https://doi.org/10.1029/2012JE004101

Liu, B., Yang, D., Ye, B., & Berezovskaya, S. (2005). Long-term open-water season stream temperature variations and changes over Lena River Basin in Siberia. *Global and Planetary Change*, *48*(1), 96–111. https://doi.org/10.1016/j.gloplacha.2004.12.007

McLean, S. R. (1992). On the calculation of suspended load for noncohesive sediments. *Journal of Geophysical Research*, *97*(C4), 5759–5770. https://doi.org/10.1029/91JC02933

McPhee, M. G. (1992). Turbulent heat flux in the upper ocean under sea ice. *Journal of Geophysical Research*, *97*(C4), 5365–5379. https://doi.org/10.1029/92JC00239

Obu, J., Westermann, S., Bartsch, A., Berdnikov, N., Christiansen, H. H., Dashtseren, A., et al. (2019). Northern Hemisphere permafrost map based on TTOP modelling for 2000–2016 at 1 km^2 scale. *Earth-Science Reviews*, *193*, 299–316. https://doi.org/10.1016/j.earscirev.2019.04.023

Ohara, N., Jones, B. M., Parsekian, A. D., Hinkel, K. M., Yamatani, K., Kanevskiy, M., et al. (2022). A new Stefan equation to characterize the evolution of thermokarst lake and talik geometry. *The Cryosphere*, *16*(4), 1247–1264. https://doi.org/10.5194/tc-16-1247-2022

Parker, G. (1978). Self-formed straight rivers with equilibrium banks and mobile bed. Part 2. The gravel river. *Journal of Fluid Mechanics*, *89*(1), 127–146. https://doi.org/10.1017/S0022112078002505

Parker, G., Shimizu, Y., Wilkerson, G. V., Eke, E. C., Abad, J. D., Lauer, J. W., et al. (2011). A new framework for modeling the migration of meandering rivers. *Earth Surface Processes and Landforms*, *36*(1), 70–86. https://doi.org/10.1002/esp.2113

Parker, G., Toro-Escobar, C. M., Ramey, M., & Beck, S. (2003). Effect of floodwater extraction on mountain stream morphology. *Journal of Hydraulic Engineering*, *129*(11), 885–895. https://doi.org/10.1061/(ASCE)0733-9429(2003)129:11(885)

Partheniades, E. (1965). Erosion and deposition of cohesive soils. *Journal of the Hydraulics Division*, *91*(1), 105–139. https://doi.org/10.1061/JYCEAJ.0001165

Patsinghasanee, S., Kimura, I., Shimizu, Y., & Nabi, M. (2018). Experiments and modelling of cantilever failures for cohesive riverbanks. *Journal of Hydraulic Research*, *56*(1), 76–95. https://doi.org/10.1080/00221686.2017.1300194

Peterson, B. J., Holmes, R. M., McClelland, J. W., Vörösmarty, C. J., Lammers, R. B., Shiklomanov, A. I., et al. (2002). Increasing river discharge to the Arctic Ocean. *Science*, *298*(5601), 2171–2173. https://doi.org/10.1126/science.1077445

Randriamazaoro, R., Dupeyrat, L., Costard, F., & Gailhardis, E. C. (2007). Fluvial thermal erosion: Heat balance integral method. *Earth Surface Processes and Landforms*, *32*(12), 1828–1840. https://doi.org/10.1002/esp.1489

Rickenmann, D., & Recking, A. (2011). Evaluation of flow resistance in gravel-bed rivers through a large field data set. *Water Resources Research*, *47*(7). https://doi.org/10.1029/2010WR009793

Roux, N., Costard, F., & Grenier, C. (2017). Laboratory and numerical simulation of the evolution of a river's talik. *Permafrost and Periglacial Processes*, *28*(2), 460–469. https://doi.org/10.1002/ppp.1929

Rowland, J., Crosby, B., Schwenk, J., Piliouras, A., & Douglas, M. (2023). Riverbank temperatures on the Selawik River, Alaska 2010-2012, and Koyukuk River, Alaska June to July 2018 [Dataset]. *ESS-DIVE*. https://doi.org/10.15485/1922885

Rowland, J., Stauffer, S., & Schwenk, J. (2019). Pan-Arctic River bank erosion and accretion, and planform metrics measured over intervals ranging from 1973 to 2016 [Dataset]. *ESS-DIVE*. https://doi.org/10.15485/1571527

Rowland, J. C., & Coon, E. T. (2016). From documentation to prediction: Raising the bar for thermokarst research. *Hydrogeology Journal*, *24*(3), 645–648. https://doi.org/10.1007/s10040-015-1331-5

Rowland, J. C., Schwenk, J. P., Shelef, E., Muss, J., Ahrens, D., Stauffer, S., et al. (2023). Scale-dependent influence of permafrost on riverbank erosion rates. *Journal of Geophysical Research: Earth Surface*, *128*(7), e2023JF007101. https://doi.org/10.1029/2023JF007101

Scott, K. M. (1978). *Effects of permafrost on stream channel behavior in Arctic Alaska (Geological Survey Professional Paper No. 1068)* (p. 19). U.S. Geological Survey.

Shepherd, R. G. (1989). Correlations of permeability and grain size. *Ground Water*, *27*(5), 633–638. https://doi.org/10.1111/j.1745-6584.1989.tb00476.x

Shur, Y., Jones, B. M., Kanevskiy, M., Jorgenson, T., Jones, M. K. W., Fortier, D., et al. (2021). Fluvio-thermal erosion and thermal denudation in the yedoma region of northern Alaska: Revisiting the Itkillik River exposure. *Permafrost and Periglacial Processes*, *32*(2), 277–298. https://doi.org/10.1002/ppp.2105

Sidorchuk, A. (1999). Gultem - the model to predict gully thermoerosion and erosion (theoretical framework). In *Sustaining the global farm* (pp. 966–972). Purdue University.

Sklar, L. S., & Dietrich, W. E. (2001). Sediment and rock strength controls on river incision into bedrock. *Geology*, *29*(12), 1087–1090. https://doi.org/10.1130/0091-7613(2001)029<1087:SARSCO>2.0.CO;2

Slusarchuk, W. A., & Watson, G. H. (1975). Thermal conductivity of some ice-rich permafrost soils. *Canadian Geotechnical Journal*, *12*(3), 413–424. https://doi.org/10.1139/t75-045

Syvitski, J., Cohen, S., Miara, A., & Best, J. (2019). River temperature and the thermal-dynamic transport of sediment. *Global and Planetary Change*, *178*, 168–183. https://doi.org/10.1016/j.gloplacha.2019.04.011

Tananaev, N. I. (2016). Hydrological and sedimentary controls over fluvial thermal erosion, the Lena River, central Yakutia. *Geomorphology*, *253*, 524–533. https://doi.org/10.1016/j.geomorph.2015.11.009

Ternat, F., Boyer, P., Anselmet, F., & Amielh, M. (2008). Erosion threshold of saturated natural cohesive sediments: Modeling and experiments. *Water Resources Research*, *44*(11). https://doi.org/10.1029/2007WR006537

21699011, 2024, 4, Downloaded from https://agupubs.onlinelibrary.wiley.com/doi/10.1029/2023JF007452 by California Inst of Technology, Wiley Online Library on [14/06/2024]. See the Terms and Conditions (https://onlinelibrary.wiley.com/terms-and-conditions) on Wiley Online Library for rules of use; OA articles are governed by the applicable Creative Commons License

Turetsky, M. R., Abbott, B. W., Jones, M. C., Anthony, K. W., Olefeldt, D., Schuur, E. A., et al. (2020). Carbon release through abrupt permafrost thaw. *Nature Geoscience*, *13*(2), 138–143. https://doi.org/10.1038/s41561-019-0526-0

UAF & USACE. (2019). *Statewide Threat Assessment: Identification of Threats from erosion, flooding, and thawing permafrost in remote Alaska communities (No. INE 19.03)* (p. 99). Denali Commission.

Vanoni, V. A. (2006). Sedimentation Engineering. *American Society of Civil Engineers*. https://doi.org/10.1061/9780784408230

Vargas-Luna, A., Duró, G., Crosato, A., & Uijttewaal, W. (2019). Morphological adaptation of river channels to vegetation establishment: A laboratory study. *Journal of Geophysical Research: Earth Surface*, *124*(7), 1981–1995. https://doi.org/10.1029/2018JF004878

Walker, J., Arnborg, L., & Peippo, J. (1987). Riverbank erosion in the Colville Delta, Alaska. *Geografiska Annaler - Series A: Physical Geography*, *69*(1), 61–70. https://doi.org/10.1080/04353676.1987.11880197

Walvoord, M. A., & Kurylyk, B. L. (2016). Hydrologic impacts of thawing permafrost—A review. *Vadose Zone Journal*, *15*(6), 1–20. https://doi.org/10.2136/vzj2016.01.0010

Wankiewicz, A. (1984). Hydrothermal processes beneath Arctic River channels. *Water Resources Research*, *20*(10), 1417–1426. https://doi.org/10.1029/WR020i010p01417

Whitefield, J., Winsor, P., McClelland, J., & Menemenlis, D. (2015). A new river discharge and river temperature climatology data set for the pan-Arctic region. *Ocean Modelling*, *88*, 1–15. https://doi.org/10.1016/j.ocemod.2014.12.012

Wilcock, P. R., Barta, A. F., Shea, C. C., Kondolf, G. M., Matthews, W. V. G., & Pitlick, J. (1996). Observations of flow and sediment entrainment on a large gravel-bed river. *Water Resources Research*, *32*(9), 2897–2909. https://doi.org/10.1029/96WR01628

Winterwerp, J. C., van Kesteren, W. G. M., van Prooijen, B., & Jacobs, W. (2012). A conceptual framework for shear flow–induced erosion of soft cohesive sediment beds. *Journal of Geophysical Research*, *117*(C10). https://doi.org/10.1029/2012JC008072

Yaglom, A. M., & Kader, B. A. (1974). Heat and mass transfer between a rough wall and turbulent fluid flow at high Reynolds and Peclet numbers. *Journal of Fluid Mechanics*, *62*(3), 601–623. https://doi.org/10.1017/S0022112074000838

Yang, D., & Peterson, A. (2017). River water temperature in relation to local air temperature in the Mackenzie and Yukon Basins. *Arctic*, *70*(1), 47–58. https://doi.org/10.14430/arctic4627

Zhang, K., Gong, Z., Zhao, K., Wang, K., Pan, S., & Coco, G. (2021). Experimental and numerical modeling of overhanging riverbank stability. *Journal of Geophysical Research: Earth Surface*, *126*(10), e2021JF006109. https://doi.org/10.1029/2021JF006109

Zhang, Y., Jafarov, E., Piliouras, A., Jones, B. M., Rowland, J., & Moulton, D. (2023). The thermal response of permafrost to coastal floodplain flooding. *Environmental Research Letters*, *18*(3), 035004. https://doi.org/10.1088/1748-9326/acba32

Zhao, K., Coco, G., Gong, Z., Darby, S. E., Lanzoni, S., Xu, F., et al. (2022). A review on bank retreat: Mechanisms, observations, and modeling. *Reviews of Geophysics*, *60*(2), e2021RG000761. https://doi.org/10.1029/2021RG000761

Zhao, K., Gong, Z., Zhang, K., Wang, K., Jin, C., Zhou, Z., et al. (2020). Laboratory experiments of bank collapse: The role of bank height and near-bank water depth. *Journal of Geophysical Research: Earth Surface*, *125*(5), e2019JF005281. https://doi.org/10.1029/2019JF005281

Zhao, K., Lanzoni, S., Gong, Z., & Coco, G. (2021). A numerical model of bank collapse and river meandering. *Geophysical Research Letters*, *48*(12). https://doi.org/10.1029/2021gl093516

Zheng, L., Overeem, I., Wang, K., & Clow, G. D. (2019). Changing Arctic river dynamics cause localized permafrost thaw. *Journal of Geophysical Research: Earth Surface*, *124*(9), 2324–2344. https://doi.org/10.1029/2019JF005060

21699011, 2024, 4, Downloaded from https://agupubs.onlinelibrary.wiley.com/doi/10.1029/2023JF007452 by California Inst of Technology, Wiley Online Library on [14/06/2024]. See the Terms and Conditions (https://onlinelibrary.wiley.com/terms-and-conditions) on Wiley Online Library for rules of use; OA articles are governed by the applicable Creative Commons License